



HAL
open science

Structure-Function Relationship of Iron Oxide Nanoflowers: Optimal Sizes for Magnetic Hyperthermia Depending on Alternating Magnetic Field Conditions

Megi Bejko, Yasmina Al Yaman, Auriane Bagur, Anthony C. Keyes Jr, Patrick Rosa, Marion Gayot, François Weill, Stéphane Mornet, Olivier Sandre

► To cite this version:

Megi Bejko, Yasmina Al Yaman, Auriane Bagur, Anthony C. Keyes Jr, Patrick Rosa, et al.. Structure-Function Relationship of Iron Oxide Nanoflowers: Optimal Sizes for Magnetic Hyperthermia Depending on Alternating Magnetic Field Conditions. *ChemPhysChem*, 2024, 25 (21), pp.e202400023. 10.1002/cphc.202400023 . hal-04204571v2

HAL Id: hal-04204571

<https://hal.science/hal-04204571v2>

Submitted on 24 Jul 2024

HAL is a multi-disciplinary open access archive for the deposit and dissemination of scientific research documents, whether they are published or not. The documents may come from teaching and research institutions in France or abroad, or from public or private research centers.

L'archive ouverte pluridisciplinaire **HAL**, est destinée au dépôt et à la diffusion de documents scientifiques de niveau recherche, publiés ou non, émanant des établissements d'enseignement et de recherche français ou étrangers, des laboratoires publics ou privés.



Distributed under a Creative Commons Attribution - NonCommercial - NoDerivatives 4.0 International License

Structure-Function Relationship of Iron Oxide Nanoflowers: Optimal Sizes for Magnetic Hyperthermia Depending on Alternating Magnetic Field Conditions

Megi Bejko^{1,2}, Yasmina Al Yaman¹, Anthony Keyes¹, Auriane Bagur², Patrick Rosa², Marion Gayot³,
Francois Weill², Stéphane Mornet^{2*}, Olivier Sandre^{1*}

¹ Univ. Bordeaux, CNRS, Bordeaux INP, LCPO, UMR 5629, 33600 Pessac, France

² Univ. Bordeaux, CNRS, Bordeaux INP, ICMCB, UMR 5026, 33600 Pessac, France

³ Univ. Bordeaux, CNRS, PLACAMAT, UAR 3626, 33600 Pessac, France

* Correspondence: olivier.sandre@enscbp.fr (OS), stephane.mornet@icmcb.cnrs.fr (SM)

Abstract

Iron oxide nanoflowers (IONFs) that display singular magnetic properties can be synthesized through a polyol route first introduced almost 2 decades ago by Caruntu et al, presenting a multi-core morphology in which several grains (around 10 nm) are attached together and sintered. These outstanding properties are of great interest for magnetic field hyperthermia, which is considered as a promising therapy against cancer. Although of significantly smaller diameter, the specific adsorption rate (SAR) of IONFs reach values on the order of $1 \text{ kW}\cdot\text{g}^{-1}$, as large as “magnetosomes” that are natural magnetic nanoparticles typically $\sim 40 \text{ nm}$ found in certain bacteria, which can be grown artificially but with much lower yield compared to chemical synthesis such as the polyol route. This work aims at better understanding the structure-property relationships, linking the internal IONF nanostructure as observed by high resolution transmission electron microscopy (HR-TEM) to their magnetic properties. A library of mono- and multicore IONFs is presented, with diameters ranging from 11 to 30 nm in a narrow size distribution. More particularly, by relating their structural features (diameter, morphology, defects...) to their magnetic properties investigated by utilizing AC magnetometry over a wide range of alternating magnetic field (AMF) conditions, we showed that the SAR values of all synthesized batches vary with overall diameter and number of constituting cores. These variations are in qualitative agreement with theoretical predictions either by the Linear Response Theory (LRT) at low fields or with the Stoner-Wohlfarth (SW) model at larger amplitudes, and with numerical simulations reported previously. More precisely, our results show a continuous (almost quadratic) increase of SAR with IONF diameter for AMF amplitudes of $20 \text{ kA}\cdot\text{m}^{-1}$ and above, whatever the frequency between 146 and 344 kHz, and a pronounced maximum at an IONF diameter of 22 nm for amplitudes of $16 \text{ kA}\cdot\text{m}^{-1}$ and below. Thank to this understanding of the impact of size and core multiplicity, stable colloidal solutions of IONPs can be synthesized with diameters targeting a SAR value adapted to the theragnostic approach envisioned.

Keywords: Magnetic nanoparticles; polyol synthesis; multicore iron oxide nanoflowers; magnetic hyperthermia; specific absorption rate.

Introduction

Iron oxide nanoparticles (IONPs) have emerged within the last decades as an important tool that can lead to novel and useful avenues towards nanomedicines which combat many medical conditions (cancers, infections...).[¹],[²],[³] Their superparamagnetic properties allow these NPs to operate as diagnostic contrast agents for magnetic resonance imaging (MRI),^[4] as well as therapeutics such as heat mediators for treatment of solid tumors by magnetic hyperthermia (MH) under an applied alternating magnetic field (AMF).^[5] In addition, the magneto-thermal effect of IONPs has been exploited as an external stimulus to trigger drug release from drug-loaded magnetic thermosensitive nanocarriers, offering both temporal and spatial control.^{[6],[7],[8],[9]} Knowing these prospective applications that could lead to advanced diagnosis and treatment, availability of water-dispersible and biocompatible IONPs with narrow size distribution and optimized magnetic properties is imperative.² Among the different available types of IONPs, iron oxide nanoflowers (IONFs) synthesized through polyol route as firstly introduced by Caruntu *et al.*,^[10] have gained attention due to their remarkable magnetic properties. These NPs are characterized by a multi-core structure as observed by transmission electron microscopy (TEM), presumably created through a mechanism of oriented aggregation of the nuclei formed by the iron oxide precursors^[11]. They appear as mono-crystals in high-resolution transmission electron microscopy (HR-TEM), as if the nuclei were sintered altogether by the growth process, which is performed at reflux in a high boiling point polyol solvent, e.g. ~220°C for diethylene glycol (DEG). This sintered morphology is thought to be the peculiarity at the origin of their high efficiency for magnetic hyperthermia,^[12] which makes them competitive even with the natural IONPs of largest diameter (~40 nm), denoted “magnetosomes”.^[13] Another advantage over magnetosomes is that these synthetic IONPs are made in a much higher yield than the bioengineered production of magnetosomes in bacterial culture. Such a structure of multiple cores linked together was shown to lead to a spin-glass state of the magnetic moments,^[14] related to their high blocking temperature (T_B) as compared to mono-core IONPs of same diameter.

In the recent years, much effort has been devoted to synthesize IONFs with optimized heating efficiency *via* synthetic routes that can offer a better control on their size, shape and crystallinity, while being compatible with scale-up for further industrial development.^[15] For this aim, the literature has shown many synthetic parameters worth investigating, including solvents of varying boiling temperatures (polyols, pure or mixed with poly(hydroxy) amines),^[16] iron oxide precursors (chlorides, nitrates, acetylacetonate...),^[17] concentration of added salts such as sodium acetate,^[18] or polymers like poly(acrylic acid),^{[19],[20]} poly(ethylene glycol) (PEG)^[21] or dicarboxy-PEG,^[22] hydro- or solvothermal pressure (*i.e.* use of an autoclave),^{[23],[24]} or multi-step (seed-growth) method to prepare core-shell IONPs.^[25] Instead of polyols, Spizzo *et al.* successfully used 2-pyrrolidone as another high boiling point polar solvent for IONF synthesis,^[26] whereas Zhang *et al.* used a polymer melt of 1000 g·mol⁻¹

PEG as reaction medium, mixed with poly(vinyl pyrrolidone) (PVP) or poly(ethylene imine) (PEI)¹⁸ as iron chelating polymers^[27]. Nikitin *et al.* studied the thermal decomposition of Fe(acac)₃ complex in benzyl ether in presence of stoichiometric amount of 1,2-hexadecanediol and of various organic acids, and also obtained IONF morphologies.^[28] Additionally, other authors reported the synthesis of multicore IONPs without the use of the polyol route, through an oxidative precipitation of iron(II) chloride in aqueous medium, in presence of carboxydextran as a chelating polymer,^[29] or by an alkaline coprecipitation of FeSO₄ and FeCl₃ with multivalent alginate chains.^[30]

Previous work by Hemery *et al.* showed the utmost important role played by adding stoichiometric quantities of water in the polyol medium for the synthesis of IONFs, so that the forced hydrolysis mechanism prevails over the reduction reaction.^[31] In the same vein, Gavilán *et al.* compared these different synthetic methods for IONFs preparation in terms of simplicity, yield, quantity produced,^[32] and drew a generalized idea on how structural and magnetic properties are interrelated in IONP systems of different morphologies.^[33] Recently, Bertuit *et al.* implemented the polyol synthesis route of IONFs in continuous flow by controlling the heating ramp to 220°C between 2°C·min⁻¹ and 8°C·min⁻¹, with a residence time in the millifluidic reactor between 1 and 2 h.^[34] Later on, these authors reported linear dependence between the SAR of IONFs with their mean number of cores (N_{core}) estimated by the ratio of the physical volume (determined by TEM) divided by the magnetic domain volume (assessed by fitting the magnetization curve with Langevin's function). The linear dependence of the heating rate with the number of grains was interpreted by the exchange energy couplings between the cores, estimated proportional to N_{core} (assuming the average number of neighbors around a given core in a cluster is constant).^[35] Nevertheless, in all the studies aforementioned, the evaluation of the heating power and its dependence with structural parameters, is generally done under limited AMF conditions of amplitude and frequency. As a result, this limitation restricts our understanding of how the magnetic field conditions alongside the intrinsic properties of the IONPs themselves can affect their heating efficiency.

Expecting this underlying relationship, we propose a thorough investigation of the structure-properties relationship existing between all the parameters known to influence the magnetic properties of IONPs: size, morphology, structural defects, composition, as well as the characteristics of the applied AMF. For this purpose, the heat efficiency was measured under a wide range of AMF conditions affording a library of IONPs and IONFs prepared by slightly changing the classic polyol conditions originally published by Caruntu *et al.*^[10] More precisely, by adding various amount of H₂O, and modifying the solvent ratio or the cooling temperature ramp, yielded a whole library of monocoresh IONPs and multicore IONFs with narrow mean size variation between the synthesized batches (less than 5 nm), with diameters ranging from 11 to 30 nm. The selected size range was intentional, since

it corresponds to sizes of interest for biomedical applications as well as to the upper and lower limits of validity of respectively LRT and Stoner-Wohlfarth theories.^{[36],[37]} In-depth multiscale characterization of the synthesized NFs was carried out, starting from their structural features (overall diameter, morphology *i.e.* mono or multicore, number and size of cores, crystal size and structural defects), chemical composition, and magnetic properties probed under a static magnetic field (saturation magnetization, blocking temperature, anisotropy energy constant, and magnetic domain size). Lastly, the heating performances of the IONPs were investigated by AC magnetometry where the specific adsorption rate (SAR, expressed in $\text{W}\cdot\text{g}^{-1}$ of $\gamma\text{-Fe}_2\text{O}_3$) was determined on a wide range of field conditions by direct integration of the hysteresis loop area A ($\text{mJ}\cdot\text{g}^{-1}$) of the dynamic magnetization curves $M(t)$ vs. $H(t)$ measured using a so-called pick-up coil instrumentation.^{[38],[39],[40]} This way, the variation of the SAR of all the synthesized batches with overall diameter (from TEM) as well as crystal size (from XRD) and magnetic domain size (from the fit of VSM curves) was evaluated under 24 different AMF conditions within reasonable experimental time. By gathering the results obtained from structural and magnetic analyses of the IONPs and of their heating power determined under a wide range of AMF conditions (amplitude from 4 to 24 $\text{kA}\cdot\text{m}^{-1}$ and frequency from 146 to 344 kHz), we were able to draw a complete picture on how all these parameters are interrelated within these systems. The results shown in this manuscript demonstrate that IONF heating efficiency varies in a complex interdependent manner. It changes not only with the size, structure and morphology of the NFs but also with the selected AMF conditions, following the predictions of either Stoner-Wohlfarth or linear response theoretical models and joining the previously reported numerical simulations of Mehdaoui *et al.*^[41] and those of Engelmann *et al.*^{[42],[43]} for the variation of SAR with sizes under various AMF conditions. As a result of this work, the limits in terms of reproducibility and yield of the polyol route for producing performant IONFs as heat mediators for MH is captured. We anticipate this expanded foundation of interdependent factors will contribute to the scaled-up and optimized production of IONPs that are more efficient for biomedical applications.

Materials and Methods

Materials

Iron (II) chloride tetrahydrate ($\text{FeCl}_2\cdot 4\text{H}_2\text{O}$, 98%), iron (III) chloride hexahydrate ($\text{FeCl}_3\cdot 6\text{H}_2\text{O}$, >97%), iron (III) nitrate nonahydrate ($\text{Fe}(\text{NO}_3)_3\cdot 9\text{H}_2\text{O}$, >98%), diethylene glycol (DEG, 99%), *N*-methyldiethanolamine (NMDEA, 99%), sodium hydroxide micro-pellets (NaOH, 98%), fuming nitric acid (HNO_3 , 69%), ethanol (EtOH), acetone, and ethyl acetate (EtAc) were purchased from Thermo Fisher Scientific (Karlsruhe, Germany) or Sigma-Aldrich (St Quentin Fallavier, France) and used without further purification.

IONP Synthesis via the Polyol Route

The original protocol by Caruntu *et al.*^[10] was reproduced, with some adjustments, particularly the addition of a controlled amount of deionized water in the medium.^[31]

- Synthesis of nanoflower batches named NF3, NF4 and NF5 through classic polyol route conditions: A mass of 1.082 g (4 mmol) of $\text{FeCl}_3 \cdot 6\text{H}_2\text{O}$ and 0.398 g (2 mmol) of $\text{FeCl}_2 \cdot 4\text{H}_2\text{O}$ is dissolved in 80 g of a liquid mixture of DEG and NMDEA with 1:1 (v/v) ratios (solution A). The resulting solution was then flushed with inert gas (N_2 or Ar) under stirring for 1 h. In parallel, 0.64 g (16 mmol) of NaOH was dissolved in 40 g solution of polyol 1:1 (v/v) in an ultrasound bath and flushed with inert gas under stirring for 1h (solution B). Then, solution B was added to solution A in a round bottom flask of 250 mL, and the resulting mixture was flushed with nitrogen or argon for 15 min and heated with a ramp of $2^\circ\text{C} \cdot \text{min}^{-1}$ up to 220°C , using an electronically controlled Digi-Mantle™ dry heater (Electrothermal™ OMCA0250) under mechanical stirring at 400 RPM with a Teflon stirring rod. After 4h of reaction at reflux, the resulting black suspension of magnetite Fe_3O_4 NPs in the round bottom flask was removed from the heating mantle, causing the sample to rapidly cool down in the air convection flow of the hood (reaching $<20^\circ\text{C}$ above RT typically in ~ 15 min), quenching the reaction. Then we proceeded with the subsequent washing and oxidation steps.
- Synthesis of NF1: For the synthesis of this batch, the quantities of $\text{FeCl}_3 \cdot 6\text{H}_2\text{O}$, $\text{FeCl}_2 \cdot 4\text{H}_2\text{O}$, NaOH and the volume ratios of DEG and NMDEA solvents to produce solutions A and B were identical to the classic polyol protocol as described in previous paragraph. However, after adding solution B to A and stirring for 10 min under inert gas, 5.5 mmol (100 μL) of H_2O was added to the mixture at room temperature, followed by stirring and flushing for 10 min with inert gas. All the following steps (heating ramp, time of reaction, cooling, washing and oxidation) were identical to the previous classical protocol.
- Synthesis of NF2: For the preparation of solution A, the same quantities of iron salts as previously were added in 80 g liquid mixture of DEG/NMDEA, but with volume ratios of 1.5:1 instead of 1:1, before being stirred under inert gas for 1h. In parallel, for the preparation of solution B, the NaOH pellets were added to 40 g of a liquid mixture of DEG/NMDEA with volume ratios of 1.5:1 and stirred under inert gas for 1h. Then, solution B was added to the solution A and the resulting mixture was flushed with inert gas for 15 min. Again, all other steps of the protocol were kept the same.
- Synthesis of NF6 and NF7: The synthetic procedure as well as the quantities of $\text{FeCl}_3 \cdot 6\text{H}_2\text{O}$, $\text{FeCl}_2 \cdot 4\text{H}_2\text{O}$, NaOH and the volume ratios of DEG and NMDEA solvents to produce solutions A and B were identical to the classical polyol protocol described in first place, together with their mixing, flushing with argon, ramp of $2^\circ\text{C} \cdot \text{min}^{-1}$ up to 220°C and 4h of reaction at reflux and 400 RPM stirring. The difference here stands in

the end of the protocol. Namely, the heating was turned off and the resulting black suspension of magnetite Fe_3O_4 NPs was left cool down slowly overnight to room temperature under inert gas flushing on the hot heating mantle. The washing and oxidation steps were done the morning after, in this case.

Washing and Isolation of the IONPs

- After each synthesis, the suspension was cooled down to room temperature (either slowly or rapidly) and poured into a 500 mL beaker and settled on large ferrite magnets ($152 \times 101 \times 25.4 \text{ mm}^3$, Calamit Magneti™, Milano-Barcelona-Paris) for 10 min. After removing all the polyol supernatant by suction, a large volume of 1:1 mixture (v/v) of EtAc and EtOH was used to wash the solid, which was re-suspended by mechanical stirring for 15 min at 200-250 RPM. After magnetic settlement, the supernatant was again removed by suction, and the nanoparticles were transferred into a smaller beaker (50 mL). The washing procedure with the EtAc/EtOH mixture was repeated 3 times to remove any organic layer covering the nanoparticles originating from polyol decomposition.

Acidification and Oxidation of the IONPs

- Next, following the method introduced by Tourinho *et al.* to progressively convert Fe_3O_4 into the oxidized phase $\gamma\text{-Fe}_2\text{O}_3$,^[44] 8.25 g of iron (III) nitrate was dissolved in 20 mL of water and boiled before adding to the pellet of nanoparticles. The resulting suspension was heated to 80°C for 45 min (maximum duration) to achieve complete oxidation of the nanoparticles (color shifts from black to brown). The suspension was decanted on the permanent magnets to isolate nanoparticles from the solution. Once the supernatant was removed by suction, another 40 mL of a 10 wt % HNO_3 (2 M) solution was added, and the resulting suspension was stirred for 10 min. After magnetic sedimentation, the supernatant was removed by suction and then replaced by acetone. After stirring for 5 min, the suspension was again magnetically decanted, and the supernatant was removed by suction. The same washing steps were repeated once with acetone and twice with diethyl ether. A final drying by suction was performed and then 20-30 mL of deionized water was added to the nanoparticles, which readily disperse. The colloidal suspension was then sonicated for 10 min (Sonics 130 W Vibracell™) to break any remaining aggregates and fully disperse the nanoparticles as a stable ferrofluid with a final $\text{pH} \sim 2$ (dilute HNO_3). The pH was maintained near this value to keep colloidal stability during any further dilution for the study of the IONP properties.

Methods for the IONP Characterization

- Determination of $\gamma\text{-Fe}_2\text{O}_3$ concentration: The solid weight concentration in iron oxide was assessed by a photometric method after mineralization of the IONPs, using the characteristic absorption peak at 350

nm of $[\text{Fe}(\text{Cl})_6]^{3-}$ complex, after an aliquot of the suspension was completely digested in concentrated hydrochloric acid (HCl 5 M), according to a previously determined calibration line.^[45]

- Ultraviolet (UV)-Visible-Near Infrared (NIR) spectroscopy: The absorbance spectra of IONPs were recorded on a Shimadzu 1800 Double Beam UV-Vis Spectrophotometer. For this, the concentration of the NPs was set at $0.32 \text{ g}\cdot\text{L}^{-1}$ ($2 \text{ mM } \gamma\text{-Fe}_2\text{O}_3$ *i.e.* 4 mM Fe^{3+}) by dilution in 10 mM HNO_3 ($\text{pH}\sim 2$). Then, 3 mL of the dispersion was put into a quartz cuvette (light path $L=1 \text{ cm}$). The spectra were then recorded from 400 to 1100 nm , using pure solvent (dilute HNO_3 at $\text{pH}\sim 2$) in the reference beam.
- Luminescence spectrophotometry: The luminescence emission spectra of IONFs were recorded on a Jasco Spectrophotometer FP-8500. The NPs were previously diluted at $0.32 \text{ g}\cdot\text{L}^{-1}$ ($2 \text{ mM } \gamma\text{-Fe}_2\text{O}_3$ *i.e.* 4 mM Fe^{3+}) in 10 mM HNO_3 and transferred in a quartz cuvette ($L=1 \text{ cm}$). The excitation wavelength was set at 232 nm with a scan speed of $100 \text{ nm}\cdot\text{min}^{-1}$ and with bandwidths of 20 nm for both excitation and emission.
- Transmission electron microscopy (TEM): Direct observation of the size, size distribution and morphology of the nanoparticles were made by TEM on a Jeol™ JEM-1400+ instrument operated at 120 kV , and digital micrographs were obtained with a Smart Orius 1000 Gatan camera. High resolution electron micrographs (HR-TEM) were obtained with a Jeol 2200FS microscope equipped with a 2k pixel Gatan Camera while selected area electron diffraction patterns (SAED) were made on a Jeol 2100 microscope equipped with an Orius 200D Gatan camera. All these microscopes are available on the PLACAMAT platform, Bordeaux. Prior to observation, the colloids ($10 \mu\text{L}$, $0.2 \text{ g}\cdot\text{L}^{-1} \gamma\text{-Fe}_2\text{O}_3$) were deposited onto TEM copper grids (lacey/thin double carbon film Cu-300LD, 300 mesh, Pacific Grid Tech, San Francisco, CA). The excess of the droplet was removed with a filter paper to leave a thin liquid film on the TEM grid. The grids were then left to dry for $10\text{-}15 \text{ min}$ before analysis by TEM.
- Image analysis: NP size distribution was obtained by measuring the diameters of ~ 300 NPs of each batch using the ImageJ software (<https://imagej.nih.gov/ij/>). Size-histograms were fit to a normal distribution law using Origin software. The morphology proportion of spherical (monocore) NPs and flower NPs (multicore) was determined by counting the number of each type of NP on the TEM images. For each batch, a total number of NPs where $N>300$ was considered to determine the morphological statistics. The constituting core diameter of the multicore NPs was determined by measuring the average size of the cores on both high magnification ($> 60000\times$) and HR-TEM images using ImageJ software. For a better estimation of the core size, the measurement was done on approximately $N\sim 250$ cores for NF3, NF4, NF5, NF6 and NF7 batches, and $N\sim 120$ for NF2.
- X-ray powder diffraction: XRPD patterns were acquired on a PANalytical X'pert MPD Pro diffractometer with Bragg-Brentano geometry, Cu $K\alpha$ radiation ($\lambda = 1.54184 \text{ \AA}$) and a secondary graphite 370

monochromator. The samples were dried, and the powder evenly spread onto a Si wafer for analysis. Patterns were analyzed with both HighScore and Eva software to obtain the crystallographic unit cell, as well as the crystal size from the Debye-Scherrer equation.

- Dynamic light scattering: DLS operated in backscattering mode *i.e.* at 165° angle (Vasco™ Flex, Cordouan Technologies™, Pessac, France) was used to calculate the hydrodynamic intensity-average size and polydispersity index (PDI) defined as the ratio of the 2nd order coefficient to the square of the 1st order coefficient in the Cumulant series analysis of the autocorrelation curves,^[46] as well as multimode Padé-Laplace algorithm.^[47] In practice, five runs of 40 s durations were acquired, and the Z-average diameter (Z_{ave}) and PDI were averaged while a standard deviation was calculated from the statistics of the five runs. Additionally, the broadness of the size distribution was estimated using $Z_{ave} \times PDI^{0.5}$ according to standard method of light scattering data analysis.^[46]
- Magnetic heating efficiency measured by AC magnetometry: Dynamic hysteresis loops were measured by AC magnetometry using a pick-up coil technology^[38] of the AC Hyster™ setup commercialized by NanoTech Solutions company (Ntsol, Madrid, Spain) that allows working under a wide range of magnetic field amplitude H varying from 4 to 24 kA·m⁻¹ with increments of 4 kA·m⁻¹ and for frequencies in the range from 10 to 344 kHz.^[48] In brief, an aliquot of 40 μL suspension in the concentration range 4-12 g·L⁻¹ (containing a dry γ -Fe₂O₃ mass of typically 1.5×10^{-7} kg) was introduced at the bottom of a 3 mm diameter 4 inches length NMR tube (VWR, France). Then the magnetization cycles $M(H)$ were measured thrice (waiting 45 s between each measurement for the sample to cool down) at a series of magnetic field amplitudes (H_{max}) ranging from 4 to 24 kA·m⁻¹ and at frequency (f) varied in this series: 146, 217, 280 and 344 kHz. The three measured cycles were averaged and normalized by the exact weight of iron oxide known from iron titration to compute the mass magnetization in A·m²·kg⁻¹. To cope with unavoidable drifts of the pick-up coil calibration, each curve $M(H)$ was adjusted by a normalization factor so that the mass magnetization measured under an AMF of amplitude $H_{max}=24$ kA·m⁻¹ was identical to the value measured by VSM magnetometry under DC magnetic field of same intensity $H_{DC}=24$ kA·m⁻¹. The validity of the SAR measurement by AC magnetometry was double-checked for some samples by also determining it *via* the classical yet much more time-demanding calorimetry method in the same AMF conditions, showing good agreement between the two methods as previously shown in literature.^{[39],[48]}
- Static magnetization curves *versus* magnetic field: DC magnetization curves $M(H_{DC})$ were recorded on a Microsense™ EZ-7 Vibrating Sample Magnetometer (VSM). For this measurement, the samples were diluted at 2 g·L⁻¹ γ -Fe₂O₃ in HNO₃ 10 mM (pH~2) and an aliquot of 20 μL was added in silver capsules for solids (Säntis AG, Switzerland) as sample holders. The magnetization was then recorded under a range of

applied magnetic field intensities H_{DC} from 0 to $H_{max}=1430 \text{ kA}\cdot\text{m}^{-1}$ ($B_{max}=1.8 \text{ T}$) with regularly spaced data points and at least 40 measurements in the low-field region ($H<475 \text{ kA}\cdot\text{m}^{-1}$ or $B<0.6 \text{ T}$).

- Static magnetization curves *versus* temperature: Zero Field Cooled (ZFC) and Field Cooled (FC) (ZFC/FC) magnetization curves were measured on a Microsense™ EZ-7 VSM under a wide temperature range (100-420K). For this, 100 μL of NPs diluted in 10 mM HNO_3 (pH~2) to $0.1 \text{ g}\cdot\text{L}^{-1} \gamma\text{-Fe}_2\text{O}_3$ were added in rectangular cotton pieces of 0.072 cm^3 ($0.6\times 1.2\times 0.1 \text{ cm}$) and then dried at 70°C for 3h, aiming to separate the IONPs by the cellulosic nanofibers and to minimize dipolar interactions in the dried state, in combination with the sufficiently low concentration used. For the ZFC measurement, the dried cotton pieces were first cooled down to $T=100 \text{ K}$ under zero applied magnetic field. Then a low magnetic field $H_{DC}=4 \text{ kA}\cdot\text{m}^{-1}$ was applied while heating from 100 to 420 K. For recording the FC curve, the sample was cooled down while applying the same magnetic field $H_{DC}=4 \text{ kA}\cdot\text{m}^{-1}$.

Results

Structural Analysis (Part 1): Overall Sizes and Morphologies of the IONPs

The synthesis of the IONPs studied in this manuscript was inspired by the polyol route originally published by Caruntu *et al.*^[10] As described in Materials and Methods, the classic polyol conditions for IONPs synthesis were repeated 3 times in order to check their repeatability by producing batches named NF3, NF4 and NF5 shown in **Figure 1(c-e)**. Physical diameters (d_{TEM}) of the NPs determined through TEM image analysis of $N\sim 300$ NPs are gathered in **Table 1** and their corresponding size histograms in **Figure S1** of Supporting Information (SI). The TEM images show the presence of flower morphology made by the aggregation of small cores into multicore NPs or “nanoflowers” (NF) as well as spherical *i.e.* moncore NPs. A morphological study on $N\sim 350$ NPs was performed on the TEM images to determine the proportions of the respective multi and moncore NPs. In all cases, as shown in the pie-charts of **Figure 1(c-e)**, the majority of produced IONPs under classical polyol conditions exhibit multicore morphology (>60%), accompanied by low size dispersity as well as narrow size variation between the batches (d_{TEM} ranging from 20.9 (NF3) to 23.2 nm (NF5), less than 2 nm variation).

Sample	d_{TEM} (nm)	d_{core} (nm)	$\langle N_{\text{core}} \rangle$	d_{XRD} (nm)	a (Å)	D_z (nm)	PDI	D_1 (nm)	D_2^* (nm)
NF1	11.8 ± 3.5	11.8 ± 3.5	1.0	10.4 ± 1.1	8.365 ± 0.01	31	0.28	14.1	154 (25%)
NF2	16.4 ± 3.7	9.30 ± 1.6	2.2	16.9 ± 2.3	8.367 ± 0.003	31	0.21	17.7	49.4 (52%)
NF3	20.9 ± 3.6	10.0 ± 2.0	6.1	20.5 ± 9.7	8.385 ± 0.01	30	0.17	32.4	-
NF4	22.2 ± 4.1	11.6 ± 3.2	5.0	20.8 ± 3.5	8.37 ± 0.01	45	0.21	29.6	78 (47%)
NF5	23.1 ± 3.5	10.6 ± 2.0	8.0	17.7 ± 1.0	8.37 ± 0.01	32	0.20	24.0	192 (22%)
NF6	28.7 ± 4.9	8.80 ± 2.3	29.7	24.4 ± 4.9	8.37 ± 0.01	77	0.25	42.7	167 (47%)
NF7	29.3 ± 8.7	13.1 ± 4.2	9.1	22.0 ± 6.0	8.38 ± 0.01	82	0.20	59.1	150 (42%)

Table 1. Values of outer diameter and core size of NPs (d_{TEM} ; d_{core}) and number of cores $\langle N_{\text{core}} \rangle$ determined by TEM image analysis, monocrystal size (d_{XRD}) and lattice parameter (a) determined by XRD analysis. The Z-average hydrodynamic diameter D_z and PDI are calculated with the Cumulant method, while D_1 and D_2 are given by Padé-Laplace algorithm (* respective weighing factor of the 2nd mode, in intensity).

To decrease the size of IONPs, two strategies involving the synthetic conditions of the polyol route were considered: (1) Prior addition of H₂O in the polyol mixture based on the previous work of Hemery *et al.*^[31] and (2) Increased DEG content. For the 1st strategy, 100 μL of H₂O representing only 0.083% of the total volume was added prior to heating as described in sub-section “Synthesis of NF1”. The slight water content in the polyol medium not only plays a key role in decreasing the size of the NPs down to 11.8 nm but also significantly decreases the ratio of multicore NPs down to 8% when compared to the classic protocol. Almost all the NPs obtained were thus monocoresh of spherical morphology, as shown on **Figure 1(a)**. This incorporation of a stoichiometric amount of water in the highly hygroscopic polyol solvent mixture has a positive effect on the “forced hydrolysis” mechanism by inducing faster nucleation of numerous nuclei, which in turn produce smaller, spherical NPs.^[31] The 2nd strategy consists in increasing the DEG content in the polyol composition without changing the concentration of NaOH and iron salts. The change of solvent ratio from 1:1 to 1.5:1 DEG/NMDEA induced a slight decrease in the diameter (batch NF2 **Figure 1(b)**) of d_{TEM} =16.4 nm) when compared to the original polyol conditions followed by a change in the morphology of the NPs. Like with the H₂O adding, increasing the amount of DEG reduced the multicore proportion of the NPs down to 27% as compared to the classic polyol conditions, with the dominant morphology being spherical monocoresh NPs (70%). This result was predictable, since reducing the amount of NMDEA, a stronger chelator than DEG for the surface of iron oxide and necessary for flower morphology, modifies the interactions between the nuclei. As reported by several works, IONF synthesis departs from classical nucleation and growth mechanism by comprising an orientated aggregation step.^{[32],[49]} In the limit where the synthesis is conducted in pure DEG, it is known to produce ultra-small iron oxide nanospheres, especially under very efficient heating in a microwave oven.^[50] Bertuit *et al.* reported similar results to us, where mixed morphologies of flower and spherical 14 nm IONPs were obtained by the use of a fast heating ramp (8°C·min⁻¹) instead.^[35] We note that besides the heating ramp, the change of solvent ratio as well as the addition of H₂O produce the same effects due to a faster nucleation step, *i.e.* decrease of size and change in morphology of the NPs.

On the opposite, producing IONPs with larger diameters than those made by the classical route is possible by increasing the heating duration of the polyol solvents. Thus, by playing on the growth and ageing times of the NPs, differences in the size of IONPs were observed when compared to the classic polyol conditions. IONPs possessing larger diameters (batches NF6 and 7 with TEM diameters of 28.7 nm and 29.3 nm, respectively **Figure 1(f-g)**) were synthesized by letting the NPs cool down slowly overnight on the heating mantle under the hood while flushing inert gas, instead of fast cooling to RT. In this case, the diameter increase is ascribed to extended reaction time by which the IONPs continue to grow by Ostwald ripening or by coalescence.^[51] Additionally, almost all the produced NPs (up to 85%) in NF6 and NF7 were multi-cores. This corresponds to a 25% increase of multicore proportion compared to the classic polyol route. When comparing how morphology yields evolve with the mean size of the NPs, a trend towards higher proportions of well-defined multicore NPs is seen when increasing their size as shown in **Figure 1 (h)**, linked to the differences between the nucleation, growth and ageing steps induced by changing the synthesis parameters. Our results confirm the report of Bertuit *et al.*^[35] showing that slower nucleation favors the synthesis of multicore NPs whereas fast nucleation produces spherical monocoresh NPs. Furthermore, the fine structural analysis by electron tomography presented in the work by Lartigue *et al.*^[52] showed that the nanoflowers synthesized through the polyol route are isotropic assemblies of merged cores, forming quasi-spherical “super-crystals”, the overall diameter of which depends directly on their number of constituting cores.

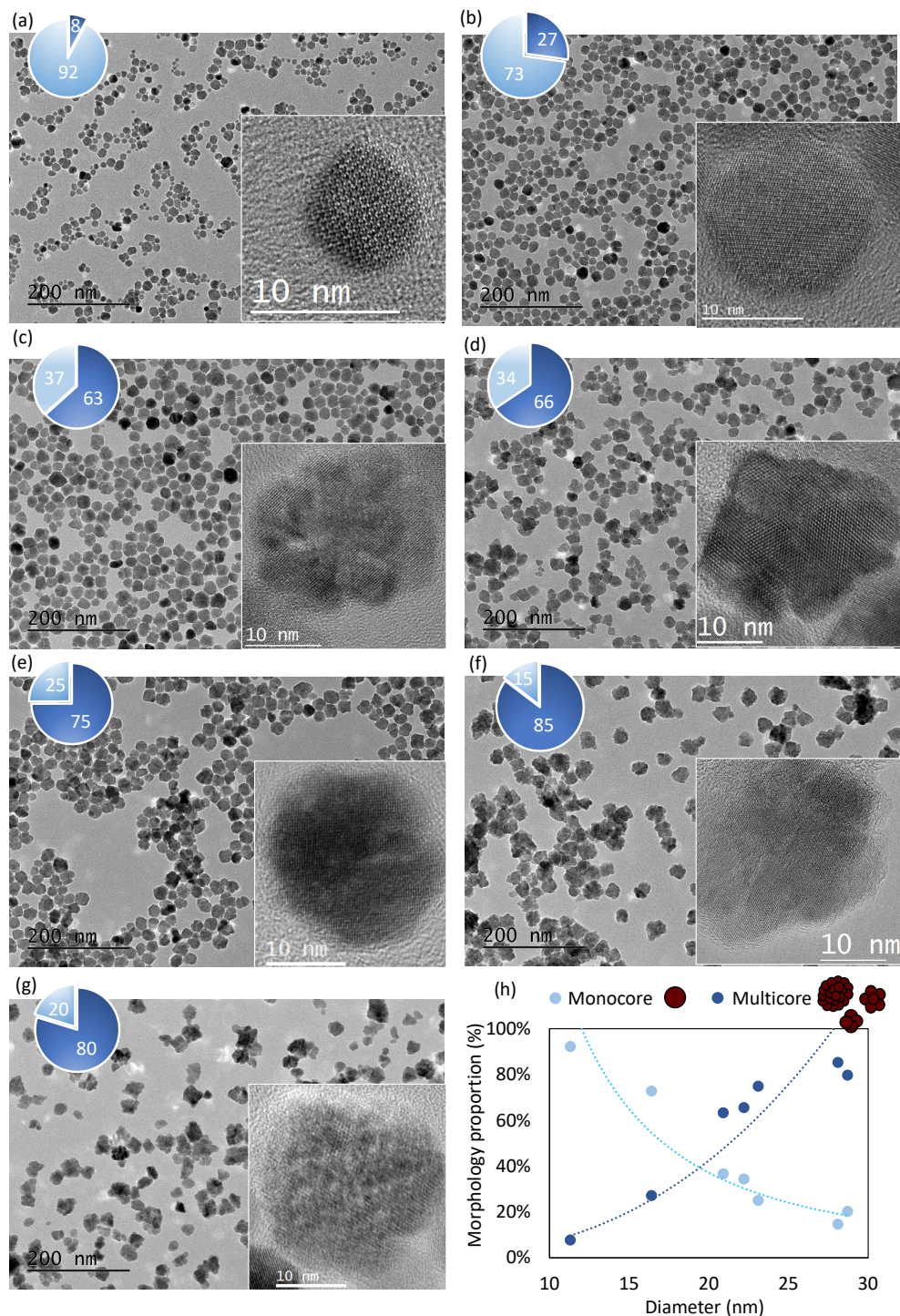


Figure 1. TEM micrographs of IONPs synthesized with (a) H₂O addition (NF1), (b) increased DEG content (NF2), (c-e) classical polyol conditions (NF3-5 respectively) and (f-g) extended reaction time (NF6-7). The pie charts show the proportion of the batches in multicore NPs (dark blue) and monocore NPs (light blue). The in-sets show HR-TEM micrographs of the IONPs. (h) Evolution of the NPs morphology with d_{TEM} . The corresponding size-histograms are gathered in **Figure S1** in Supplementary Information (SI).

The TEM image analysis allows to estimate not only the overall diameter of the IONPs (d_{TEM}), but also the diameter of the individual cores composing the nanoflowers, d_{core} . Thus, the latter was evaluated by manual counting on TEM images of $N \sim 250$ NPs for batches NF3-7 and of $N \sim 150$ NPs for NF4, due to its lower proportion in flowerlike NPs (27%, **Figure 1(b)**). Following Bertuit et al,^[35] the number of cores was estimated by the ratio:

$$N_{\text{core}} = (d_{\text{TEM}}/d_{\text{core}})^3 \quad \text{Eq. (1)}$$

Please note that this equation does not include a prefactor corresponding to compacity ratio, because the nuclei are supposed to be sintered together through atomic diffusion, causing the internal porosity of IONF to be null, unlike other types of multicore IONPs like “raspberries” reported by Gerber et al that are really close-packed clusters of spherical nuclei.^[53] For better approximation of the mean core number on the polymorphous samples, the spherical proportion was also considered through its core number as $N_{\text{core}}^{\text{S}}=1$, and a mean number of cores per dispersed object $\langle N_{\text{core}} \rangle$ was calculated for each NF sample, taking into account the proportions of the two morphologies obtained by TEM image analysis (thus a number-average). For instance, the NF6 batch with 85% of flowerlike multicore NPs with $N_{\text{core}}^{\text{F}}=34.8$ and 15% of quasi-spherical NPs defined by $N_{\text{core}}^{\text{S}}=1$ gives a mean core number $\langle N_{\text{core}} \rangle = 85\% \times 34.8 + 15\% \times 1 = 29.7$. From the values of d_{core} and N_{core} gathered in **Table 1**, one can notice that all the samples exhibit similar $d_{\text{core}} \sim 10$ nm (apart from NF7). This leads to a variation of $\langle N_{\text{core}} \rangle$ as a function of the external diameter of the NPs roughly as a power law of exponent ~ 3 versus d_{TEM} (**Figure S2** of Supporting Information SI) as if nanoflowers resulted from the sintering of nuclei with all more or less of the same unit size.

Colloidal Stability of the IONPs

The dispersion state of the different IONPs batches was assessed by dynamic light scattering (DLS) in a weakly acidic aqueous medium (10 mM HNO₃ pH \sim 2) to ensure that they bear repulsive positive surface charges. Due to their multimodal size distribution and mixed morphologies, the hydrodynamic diameters D_{H} of the batches were estimated both from the Cumulant analysis, yielding the Z-average (D_{Z}) and PDI, and from the Padé-Laplace algorithm, all the values being gathered in **Table 1**. The Padé-Laplace algorithm, more adapted for multimodal NP distribution, indicates the presence of two populations (D_1 and D_2): a main class of NPs with hydrodynamic sizes D_1 in agreement with d_{TEM} for all batches, and a second population of larger NPs, smaller in number yet highly contributing to the scattered light intensity in DLS. The Z-average values are found in between D_1 and D_2 and range from 30 nm (NF1) to 82 nm (NF7). PDI values higher than 0.20 indicate sample polydispersity, related to their broader size distribution as well as mixture of morphologies or slight aggregated state, as evidenced by TEM. Interestingly, sample NF1 has the largest PDI, even when compared to sample NF7, the latter having the largest size distribution as evaluated by TEM (**Figure S1 (g)**). This indicates that the high polydispersity of NF1 is a direct

consequence of the presence of several size populations as shown in **Figure 1(a)** as well as the presence of a low proportion of aggregates scattering light much more than smaller NPs (from the Rayleigh law of scattering according to the sixth power of particle radius) and thus contributing way more to the D_z intensity-weighting.^[46] In addition, the large D_z recorded for NF6 and NF7 is ascribed to the presence of a small proportion of exceptionally large NPs, as evidenced by D_z in the Padé-Laplace calculation.

Structural Analysis (Part 2): Crystalline Structure and Composition of the IONPs

To get a better insight on the crystal structure of the studied samples, electron (SAED) as well as X-ray (XRPD) diffraction measurements were performed on all of them. Detailed SAED patterns of the sample library are shown in **Figure S3**. For all the samples, the observed reflections are consistent with cubic lattice of Bravais type F and unit cell size ~ 8.37 Å. Please note that the intrinsic precision in determining the lattice parameters by electron diffraction does not allow detecting any difference of crystallographic cell parameter from one sample to another. Similarly, the XRPD patterns (**Figure S4 (a)**) were identical for all the NF series. The reflections match with the expected Bragg peaks of magnetite Fe_3O_4 . Both diffraction techniques do not permit the validation of the oxidation step of IONPs as maghemite and magnetite forms crystallize in the same space group, only differing by the oxygen vacancy order. However, the XRD patterns give us information on the lattice parameter as well as the crystal size of IONPs. The lattice parameters a retrieved by XRD data refinement are gathered for all NP batches in **Table 1**. The cell parameters of all samples lie in between the values of bulk maghemite (8.346 Å, JPCDS 39-1346) and bulk magnetite (8.396 Å, JCPDS 19-0629), indicating that the oxidation step is incomplete, leaving magnetite rich zones within the samples. Furthermore, many reports have shown that the oxidation step of IONPs is a size-dependent process, with maghemite being the dominant phase of small-sized NPs when compared to larger ones.^{[54],[55]} An easy way to assess the oxidation state of NPs and its evolution with size consists in monitoring the near-IR (NIR) band above 1000 nm assigned to intervalence charge transfer (IVCT) between Fe^{2+} and Fe^{3+} in magnetite only.^[56] The loss of the NIR band indicates progressive oxidation of the magnetite phase Fe_3O_4 into maghemite $\gamma\text{-Fe}_2\text{O}_3$. The visible-NIR absorbance spectra were recorded for IONPs NF1, NF2, NF3, NF5 and NF6 with sizes (d_{TEM}) 11.8, 16.4, 20.9, 23.1 and 28.7 nm respectively, to check the evolution of magnetite content with size. As shown by the absorption spectra in **Figure S4 (b)**, the lowest optical absorbance in the NIR region was recorded for the smallest sample NF1, indicating the highest content of maghemite amongst the series, as expected. On the other hand, the optical absorbance in the NIR increases progressively with size. Samples NF2 (16.4 nm), NF3 (20.9 nm), NF5 (23.1 nm) and NF6 (28.7 nm) exhibit higher molar extinction coefficients (defined from the atomic Fe content) in the NIR, indicating higher content in magnetite when compared to NF1.

From the XRPD data, crystalline domain sizes for the IONPs were deduced from the peak broadening effect by applying the Scherrer equation on the most intense peaks of the diffractograms:

$$\tau = \frac{k\lambda}{\beta \cos(\theta)} \quad \text{Eq. (2)}$$

where k is the form factor (0.89 for spherical NPs), λ the X-ray wavelength, β the peak full width at half maximum (FWHM) intensity, and θ the Bragg diffraction angle.

With this formula, crystal sizes (d_{XRD}) of 10.4 and 16.9 nm were estimated for NF1 and NF2 respectively, values quite close to their TEM core sizes (~ 11.8 and 16.4 nm), suggesting that these batches, mainly composed of spherical NPs, are monocrystalline. Similarly, for the larger IONPs possessing high proportions of multicore NPs (from NF3 to 7), the crystal size is most of the time close to the TEM outer diameter d_{TEM} . This indicates that the small cores may have gone through an epitaxial growth and share the same crystal orientation, a growth mode called “oriented aggregation” firstly reported for iron oxyhydroxide nanocrystals.^[11] HR-TEM images showed in **Figure 1** confirm the results obtained by XRPD as for each sample, continuous crystallinity throughout the volume of the flower was observed.

Inverse fast Fourier transform (iFFT) analysis of the HR-TEM images enables distinguishing crystalline defects present on different crystal planes for all the set of IONPs. **Figure 2** compares the (220) crystal plane of samples: NF1 and NF2 composed mostly by moncore NPs and NF4 and NF6 by multicore NPs. The iFFT images of NF1 and NF2 present no defects within the crystal plane (220) as shown in **Figure 2 (c)** and **(f)**. On the other hand, the iFFT images of NF4 and NF6 (**Figure 2 (i)** and **(l)**), which correspond to samples of predominant multicore morphology yet very different values of $\langle N_{\text{core}} \rangle$, demonstrate the presence of misalignments (disclinations) in the (220) plane. One notes that these structural defects are predominant in multicore NPs and localized near the surface borders (as shown for NF3 and 4 in **Figure S5 (c)** and **(f)**) or within the structure, near the borders of the constituting cores (as shown in **Figure S5 (i)** for NF6). However, since beam-related artefacts may occur during HR-TEM analysis, the presence of structural defects was evidenced through fluorescence spectroscopy as well, by recording the NP emission after UV excitation at 232 nm. For all the set of NPs, a main peak centered at ~ 560 nm was observed as shown in **Figure S6 (a)** and **(b)**, as ascribed to the presence of interstitial oxygen atom defects.^{[35],[57],[58],[59]} Based on the report of Sadat *et al.*, the observed photoluminescence (PL) is due to radiative recombination of mobile electrons from e_g to t_{2g} on octahedral sites of iron oxide.^[60] Bertuit *et al.* has recently reported that the PL intensity of IONPs is highly enhanced with the concentration of emitting defects.^[35] In our case, the maximum PL intensity increases linearly with the $\langle N_{\text{core}} \rangle$ number as shown in **Figure S6 (c)**. Interestingly, when normalized with the $\langle N_{\text{core}} \rangle$ concentration, the maximum PL intensity increases with d_{TEM} following a power law of exponent around 2

(illustrated in **Figure S6 (d)**). This indicates that the PL intensity as well as emitting defect concentration varies as the area of the NF outer surface, in good correlation with the defect study by HR-TEM showing misalignments near the NF surface, with larger NPs of higher $\langle N_{\text{core}} \rangle$ possessing higher defect occurrence than monocoresh NPs. It is worth noticing that NF6, which has the largest diameter as well as $\langle N_{\text{core}} \rangle$ number, emits also the highest PL intensity under UV when compared to all other samples. Furthermore, NF4 (22.2 nm) exhibits also higher PL intensity indicating higher defect density when compared to analogous batches NF3 (20.9 nm) and NF4 (23.4 nm).

Then higher occurrence of defects in multicore NPs also gives insights on their nucleation and growth mechanisms. For multicore NPs, once small nuclei form in the polyol mixture, they are prone to aggregation to minimize their high surface energy. When they get in close contact, these small cores rotate relatively to each other until they share the same crystal orientation as their neighbors, and they start to get sintered by atomic diffusion, which is enhanced by the high temperature. This so called “oriented aggregation” process creates multicore NPs yet gives rise to small crystal defects in between the cores forming the NP. However, these topologic defects (such as disinclination lines or planar inclusions) are insufficient to create real grain boundaries, as all the cores share the same crystallographic orientation of their atomic planes. One could argue against this scenario that dipolar repulsion at long range between magnetic domains of same orientation plays against their merging into a single monodomain. But although the reaction temperature (220°C) is still far below the Curie temperature of iron oxide in the bulk, the thermal agitation is high enough to cause the collision of nuclei at a sufficiently close distance (~1 nm) so that the exchange energy can override this barrier, given also the fact that magnetic moments of nuclei are still small enough so that their dipolar energy when at contact stays of the same order of magnitude than $k_B T$. On the other hand, spherical NPs follow a more classical pathway including rapid nucleation and growth towards a single crystal structure by diffusion of oxide precursor species from the solution to the nuclei surface.^[50]

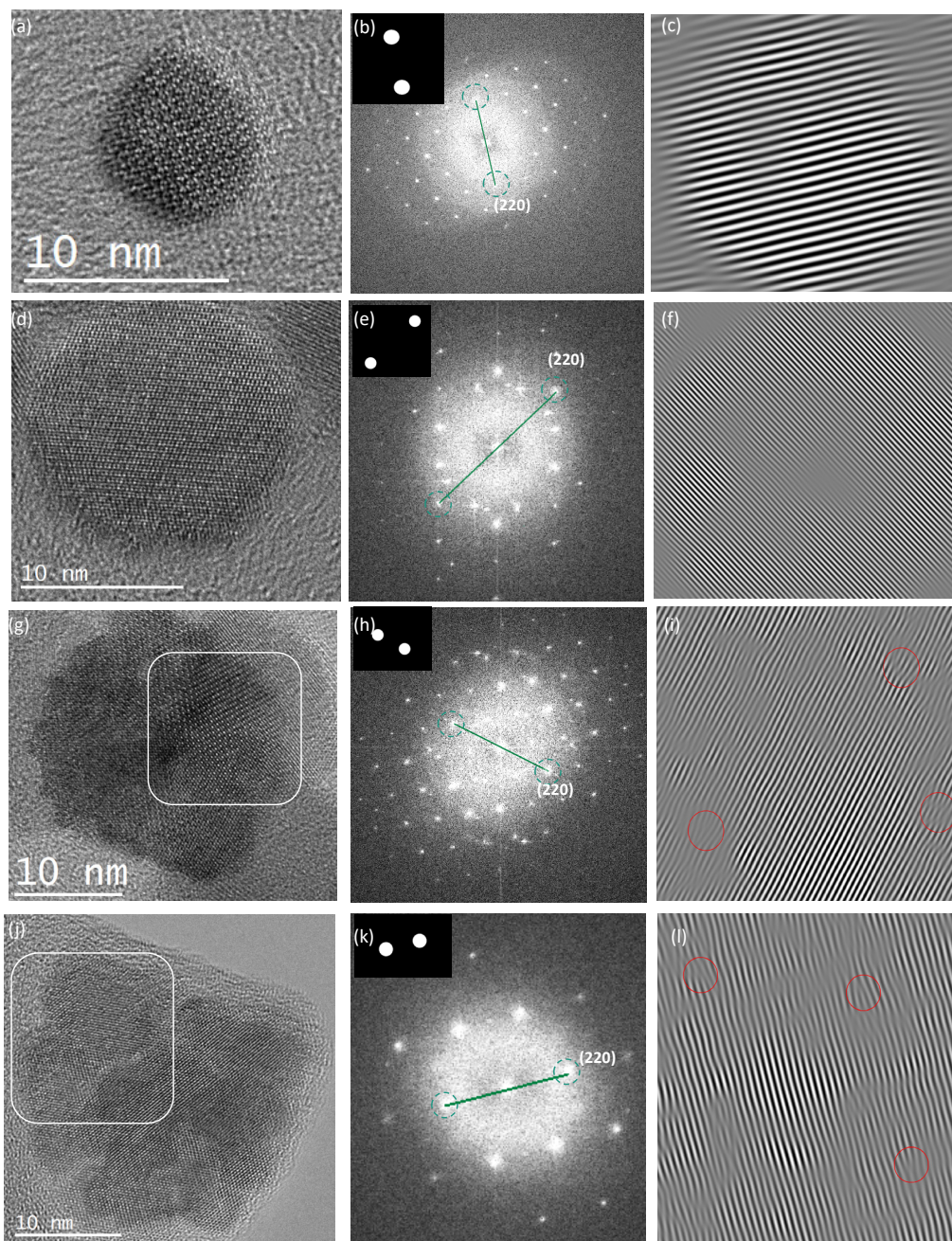


Figure 2. HR-TEM images of batches (a) NF1 (d) NF2, (g) NF4 and (j) NF6. (b), (e), (h) and (k) Fast Fourier Transformation (FFT) images obtained from HR-TEM images respectively. The inset shows the masks used to highlight the (220) planes in the FFT images. (c), (f), (i) and (l) are inverse FFT images of the (220) planes of NF1, 2, 4 and 6 selected in the FFT images, respectively. Please note that (i) and (l) correspond to the zones depicted by the white squares in (g) and (j), respectively. Red circles depict the misalignments in (i) and (j).

Magnetic Properties (Part 1): Static Magnetization Curves of the IONPs

DC Magnetometry was performed with a vibrating sample magnetometer (VSM) at $T=293$ K on water dispersions after the NF oxidation to determine the specific saturation magnetization M_s . The M vs. H curves under static field of all NPs are plotted in **Figure 3**. It can be noticed that all the NF batches have M_s ranging from 300 up to 400 $\text{kA}\cdot\text{m}^{-1}$, which are classical values for ferrite NPs (the bulk magnetization being 400 $\text{kA}\cdot\text{m}^{-1}$ for maghemite and 500 $\text{kA}\cdot\text{m}^{-1}$ for magnetite). Contrary to what is reported in literature for spherical IONPs,^[54] the highest values of M_s (377 and 415 $\text{kA}\cdot\text{m}^{-1}$), close to that of bulk $\gamma\text{-Fe}_2\text{O}_3$, was observed for the smallest samples (NF1 and 2 respectively). After closer investigation of M_s variation amongst samples, we noticed an approximately linear decrease with the proportion of multicore NPs and the mean number of cores $\langle N_{\text{core}} \rangle$, as shown respectively in **Figure 3 (d)** and **S7**.

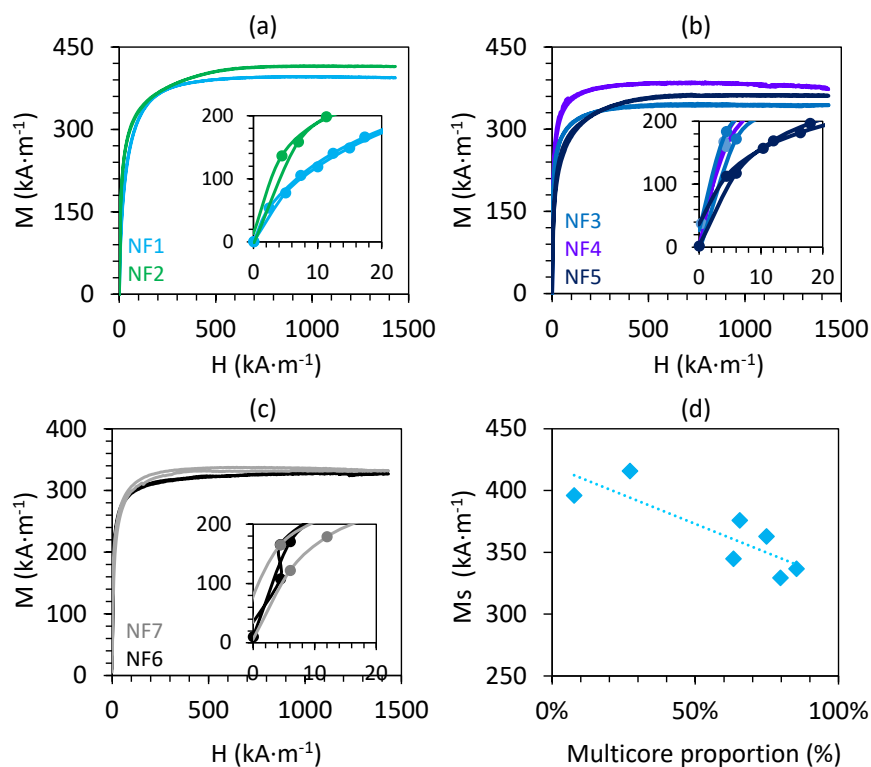


Figure 3. (a-c): Magnetization curves of IONPs recorded at $T=293$ K. The inset shows the initial magnetization of the NPs at low applied field. (d) Specific saturation magnetization M_s variation with flower-like NP proportion within the IONP batches.

As detailed in previous section, the spherical NPs possess a lower number of defects in their crystalline structure, contributing to higher M_s values, close to that of the bulk phase (case of NF1 and 2). On the other hand, the largest NPs possessing the highest multicore proportions exhibit the lowest M_s value (*i.e.* NF6 with the largest size and $\langle N_{\text{core}} \rangle$ number) owing to higher occurrence of defects affecting the overall crystal integrity as aforementioned,

inducing spin disorder. Our results follow the report of Levy *et al.*,^[61] as well as the recent study of Shingte *et al.*,^[62] which clearly demonstrate that lattice defects affect the magnetic moment magnitude and dynamics, resulting in lower magnetization and magneto-crystalline anisotropy energy both for spherical and cubic morphologies.^[61] In addition, we notice that the remnant magnetization M_r is negligible for batches NF1-6, confirming pure superparamagnetic state of the IONPs from 11.8 to 28.7 nm at room temperature as shown in the insets of **Figure 3 (a-c)**. On the other hand, sample NF7 of 29.3 nm diameter shows a slight opening of the magnetization curve into a hysteresis loop characterized by a M_r value of $81 \text{ kA}\cdot\text{m}^{-1}$ at 293 K and zero applied field. This indication of ferromagnetic contribution in the sample is either due to the presence of large NPs as evidenced by the size histogram in **Figure S1** or because, unlikely to all other flowerlike batches, its average grain size is significantly larger ($d_{\text{core}} \sim 13 \text{ nm}$ as compared to d_{core} of 9-10 nm for all the other ones, including NF6).

For the NFs belonging to the superparamagnetic regime, the magnetization curves can be described by the Langevin function convolved with a Log-normal distribution of diameters, as shown below:²⁷

$$M = M_s \int_0^\infty \delta d \cdot P_{d_0, \sigma}(d) \cdot L\left(\mu_0 \frac{M_d V_M}{k_B T} H_{\text{app}}\right) \quad \text{Eq. (3)}$$

$$\text{with } P_{d_0, \sigma}(d) = \frac{1}{d \cdot \sigma \sqrt{2\pi}} \exp\left(-\frac{(\ln(d) - \ln(d_0))^2}{2\sigma^2}\right) \quad \text{Eq. (4)}$$

Where μ_0 is the vacuum magnetic permeability, H_{app} the intensity of the applied field, M_d the magnetic domain magnetization, $V_M = \frac{\pi d^3}{6}$ the magnetic core volume for a spherical particle of diameter d , T being the absolute temperature and k_B the Boltzmann constant. Also, $P_{d_0, \sigma}(d)$ corresponds to the nanoparticle size distribution fitted by a log-normal law where d_0 is the median value of the distribution and σ the standard width of the log values. The integral on diameters d is calculated numerically for a finite increment $\delta d = 0.1 \text{ nm}$ and only d_0 and σ as adjustable parameters (the domain magnetization being simply $M_d = M_s \cdot \rho$, where M_s is the saturation magnetization per mass of iron oxide and is $\rho = 4800 \text{ kg}\cdot\text{m}^{-3}$ the mass density of the solid (taken as the tabulated value for maghemite). The results of fitted data are shown in **Figure S8** for all NFs.

From the Langevin fits on the experimental data of $M(H)$ and the specific relations of the log-normal law, we obtain the mean number-averaged magnetic size of the NPs:

$$d_{\text{VSM}}^n = d^n = \langle d \rangle = d_0 \exp\left(\frac{\sigma^2}{2}\right) \quad \text{Eq. (5)}$$

$$\text{with its standard deviation: } \quad \text{Std}(d) = d^n \sqrt{\exp(\sigma^2) - 1} \quad \text{Eq. (6)}$$

The size distribution obtained by the Langevin fit can also be weighted by the volume fraction of the NPs expressed as $\Phi(d) = P_{d_0,\sigma}(d) \cdot d^3$ (see histograms on **Figure S8**) to obtain the volume or weight-averaged magnetic diameter:

$$d_{\text{VSM}}^w = d^w = \left\langle \frac{d^4}{d^3} \right\rangle = d_0 \exp\left(\frac{7\sigma^2}{2}\right) \quad \text{Eq. (7)}$$

Table 2 gathers the obtained magnetic sizes at room temperature for all the set of NFs. For the smallest sample NF1, a minute difference is found between $d_{\text{TEM}}=11.8$ nm, $d^w=10.5$ nm and $d^n=8.1$ nm. On the opposite, there is a notable shift between d^w and d^n for larger samples presenting higher proportions of multicore morphologies. For these samples (NF2 to 6), d^n values correspond – within experimental uncertainty – to sizes close to the small unit core diameters d_{core} as determined manually from TEM images. Moreover, for most samples the d^w values corresponding to the overall magnetic size of the multicore NPs are in good accordance with their outer diameter d_{TEM} , as well as with the crystal diameter d_{XRD} . Only for NF5, the d^w value is smaller than d_{TEM} . This can be ascribed to a possible dead magnetic layer around the magnetic monodomain. Another explanation could arise from the fact that, in electron microscopy, only a fraction of the IONPs (a few hundred) contribute to the histogram of diameters while in VSM, all the NPs in the sample (*i.e.* trillions) contribute to the final average values of the diameter.^{[39],[63]} Furthermore, the initial magnetic susceptibility χ at low applied field was determined for all the set of NF suspensions by taking the initial slope of the magnetization curves (see insets of **Figure 3** zooming in the region $H_{\text{DC}} < 25 \text{ kA} \cdot \text{m}^{-1}$). The values, gathered in **Table 2**, are comprised between 15 and 40 and correspond to the extremely high χ range previously reported in the literature for IONFs.^[31]

Magnetic Properties (Part 2): Static Magnetization Versus Temperature

The VSM setup enables also to conduct ZFC/FC experiments in order to determine the blocking temperature T_B as well as the effective magnetic anisotropy constant K_{eff} of the NPs, known as a determinant parameter for magnetic hyperthermia.^[64] For this aim, samples with distinct outer TEM diameters of 11.8, 16.4, 20.9, 28.7 and 29.3 nm (NF1, 2, 3, 6 and 7) were selected. An aliquot of each batch of NPs was absorbed and dried in rectangular cotton pieces at low $\gamma\text{-Fe}_2\text{O}_3$ concentration to decrease as much as possible magnetic dipolar interactions between the IONPs by separating them with the cellulosic nanofibrils. This point could have been verified by measuring at least one batch at several concentrations, but due to limited access to the VSM magnetometer we did not perform this control experiment. In addition, the use of dried cotton pieces instead of common solvents to disperse the IONPs allows measuring curves over a broad range of T (from 100 K to 420 K) without observing the noise coming from the solvent melting point. The ZFC/FC curves shown in **Figure S9** and **S10** display two characteristic temperatures: at the maximum of the ZFC curve (T_{max}) as well as the branching temperature (T_{bra}) where the ZFC and FC curves start separating. At $T > T_{\text{bra}}$, the ZFC and FC curves are well superimposed as all magnetic moments relax, driven by

thermal fluctuations.^[65] A shift of these two temperatures towards higher values was observed with the increase of the IONP outer size. Furthermore, for monodisperse IONPs, T_{max} corresponds to the blocking temperature T_B of the magnetic moments. However, this is not the case for these samples due to non-neglectable size distribution. To accurately estimate the average blocking temperature $\langle T_B \rangle$, a method adapted for polysized samples reported by Micha *et al.* and Bruvera *et al.* was applied.^{[66],[67]} For this aim, the derivative of the difference between ZFC and FC *versus* T was plotted for each sample as shown in the **Figure S9** and **S10**. Then $\langle T_B \rangle$ was determined from the maximum of the $\delta(M_{ZFC}-M_{FC})/\delta T$ plot. For the smallest samples rich in spherical monocoresh IONPs (NF1 and NF2), the presence of only one broad peak was observed and its maximum identified as the $\langle T_B \rangle$ of these samples. On the other hand, for samples NF3, NF6 and NF7 where multicore IONPs with sizes from 20.9 to 29.3 nm dominate, up to 3 peaks appeared on the derivative plot, as illustrated in **Figure S9** (NF3) and **S10** (NF6-7). The presence of several peaks in the T dependence of the ZFC-FC derivative has already been reported for spherical or octopod-like morphologies^[68], as well as for Fe_3O_4 or $\gamma-Fe_2O_3$ nanoflowers^[31]. Based on these reports, we ascribed the broad intense peak (peak denoted as 1) to the IONP mean blocking temperature $\langle T_B \rangle$. Two hypotheses can explain the presence of the additional peaks on the derivative curves of NF3, 6 and 7. The first cause could be the contribution of the smallest NPs within the sample or the individual magnetic domains, inducing other blocking processes at T much lower than the average $\langle T_B \rangle$ (peak noted 2 for NF6 and 7). The second hypothesis concerns the presence of magnetite within the largest IONPs, as evidenced previously by XRD and NIR optical absorption, giving rise to so-called Verwey transition at T_V close to 120 K for bulk magnetite. This insulator-conductor transition induces the appearance of an additional bump in the ZFC/FC curves as seen for NF3 and NF6 around 150 K (**Figure S9** and **S10**) and leads to the presence of a supplementary peak (noted 2 for NF3, and 3 for NF6 and 7) in the derivative curves. However, confirmation of these hypotheses requires further experiments such as Mössbauer spectroscopy, EELS analysis, AC susceptibility *vs.* T etc., which are beyond the scope of this report.

The values of the mean blocking temperature $\langle T_B \rangle$ are gathered in **Table 2**. The $\langle T_B \rangle$ of samples NF1 to 3 are in between 200-300 K, proving that the IONPs exhibit superparamagnetic behavior at ambient temperature. The large $\langle T_B \rangle$ (>420 K) seen for sample NF7, was expected due to its ferromagnetic contribution as seen in the DC magnetization curve. Interestingly, the $\langle T_B \rangle$ of NF6 is situated at 415 K, well above room temperature, even though its DC magnetization curve indicated a superparamagnetic behavior at 300 K. The large $\langle T_B \rangle$ can thus be explained either by intra-particle interactions *i.e.* within the cores, enhanced for NF6 due to its high $\langle N_{core} \rangle$ number, or by inter-particle *i.e.* dipolar interactions. The latter are less probable since an extremely low IONP number density $C_{NP} = 2.4 \times 10^{12} \text{ NP}\cdot\text{cm}^{-3}$ was used for the ZFC/FC experiments, as explained in Materials & Methods section. Estimating the mean inter-particle distance $\langle r \rangle = (3/(4\pi C_{NP}))^{1/3} = 465 \text{ nm}$, the IONPs are too distant for dipole-dipole interactions to play a role.^[69] Furthermore, the plotting of $\langle T_B \rangle$ as a function of the overall magnetic

domain size d^w shows linear dependency as illustrated on **Figure 4 (a)** (power law with exponent ~ 1). On the other hand, the plot of $\langle T_B \rangle$ versus number $\langle N_{core} \rangle$ of cores composing the IONPs shows progressive increase of $\langle T_B \rangle$, following a power law with an exponent of 0.24 (**Figure 4 (b)**). It is known that $\langle T_B \rangle$ increases with the size of the NPs. However, as previously mentioned, another contribution to the large $\langle T_B \rangle$ of multicore morphologies can arise from the presence of strong exchange coupling interactions between the cores, which favor high $\langle N_{core} \rangle$ clusters with ferromagnetic order between the grains, a much rarer magnetic behavior once coined by the term “superferromagnetism”,^[70] which is still an intense field of research towards ordered networks of magnetic NPs.

From the value of $\langle T_B \rangle$, the effective anisotropy constant K_{eff} was determined for each NP using the classical (yet empirical) formula of the mean energy barrier: $\Delta E_{an} = 25k_B T_B = K_{eff} V_m$, k_B being the Boltzmann constant and V_m the magnetic volume deduced from $V_m = \pi(d^w)^3/6$. From the values of K_{eff} gathered in **Table 2** and the plot of K_{eff} vs. d^w in **Figure 4(c)** showing fast increase of K_{eff} towards small diameters, we can propose a similar interpretation as for spherical IONPs.^[54] This trend could be ascribed to higher contribution of surface anisotropy caused by the breaking of the symmetry and a reduction in the nearest neighbor coordination number at the surface for smaller diameters.^[71] However, when considering the magneto-crystalline energy barrier $\Delta E_{an} = K_{eff} V_m$ the highest value is obtained for the IONPs with $d_{TEM} = 28.7$ nm, which is twice as large as the ΔE_{an} of sample NF1 (**Table 2**). On the other hand, the effective K_{eff} constant decreases with $\langle N_{core} \rangle$ following a power law of negative exponent ~ -0.5 as shown in **Figure 4(d)**.

As simple approximation, we can make the analogy with the method developed for spherical NPs of diameter d ,^[54] by which the surface and volume contributions to the effective anisotropy constant K_{eff} are given as the sum:

$$K_{eff} = K_V + (S\sigma/V) K_S = K_V + (6\sigma/d) K_S \quad \text{Eq. (8)}$$

where $S = \pi d^2$ and $V = \pi d^3/6$ are the surface and the volume of the particle respectively, K_V the bulk anisotropy energy per unit volume, σ value measuring the deviation from a perfect sphere for which $\sigma=1$ and K_S the surface density of anisotropy energy.^[71] The dependence between K_{eff} and the inverse of magnetic domain size ($1/d^w$) is linear as expected from the Eq. (8) above (inset **Figure 4 (d)**). From this linear regression, values of $K_V = 4.85 \times 10^4$ J·m⁻³ and $K_S = 2.5 \times 10^{-4}$ J·m⁻² were found by considering our whole set of NFs. K_V appears to be one magnitude higher than the bulk anisotropy value of maghemite (4.6×10^3 J·m⁻³) but agrees perfectly with reported values of K_V in literature for spherical maghemite NPs.^{[54],[72],[73],[74],[75]} As for K_S , its value of is one magnitude higher than reported values of surface anisotropy for spherical maghemite NPs (comprised between $2 - 4 \times 10^{-5}$ J·m⁻²). This can be ascribed to the highly corrugated morphology of IONFs which were shown by Hemery *et al* to exhibit much larger specific surface area (as measured in the wet state by small angle neutron scattering) as compared to

perfectly smooth spheres of identical sizes.^[31] Furthermore, the anisotropy fields H_K calculated by the classical two-state model $H_K=2K_{\text{eff}}/\mu_0M_s$ were determined for all the set of samples and their values gathered in **Table 2**.

Sample	d^w (nm)	d^n (nm)	χ	M_s (kA·m ⁻¹)	$\langle T_B \rangle$ (K)	K_{eff} (10 ⁴ J·m ⁻³)	ΔE_{ani} (10 ⁻²⁰ J)	H_K (kA·m ⁻¹)
NF1	10.5	8.1	15.4	395.8	187	9.80	6.46	394
NF2	14.2	4.7	23.1	415.7	220	4.76	7.60	182
NF3	19.9	7.9	29.7	344.6	325	2.38	11.2	110
NF4	19.3	9.4	40.4	375.8	N.D.	N.D.	N.D.	N.D.
NF5	14.0	6.1	19.3	362.8	N.D.	N.D.	N.D.	N.D.
NF6	24.8	5.7	26.1	329.3	415	1.80	14.3	86.8
NF7*	N.A.	N.A.	19.3	336.5	>420	>6.89	>14.5	>326

Table 2. Summary of weight-averaged VSM diameters d^w , number-averaged VSM diameters d^n , magnetic susceptibilities χ , specific saturation magnetizations M_s , blocking temperatures $\langle T_B \rangle$, effective magnetic anisotropy constants K_{eff} , anisotropy fields H_K and anisotropy energy barriers ΔE_{ani} obtained respectively by Langevin fits of the DC magnetization curves obtained by VSM at RT and ZFC/FC curve analysis from 100 to 420 K under applied bias field $H_{\text{DC}}=4$ kA·m⁻¹. *This sample exhibits slight magnetization hysteresis at room temperature and therefore the DC $M(H)$ curve could not be fitted by Langevin law and thus d^w and d^n values are not available (N.A.). N.D.: not determined (as these samples were not selected for ZFC/FC measurements).

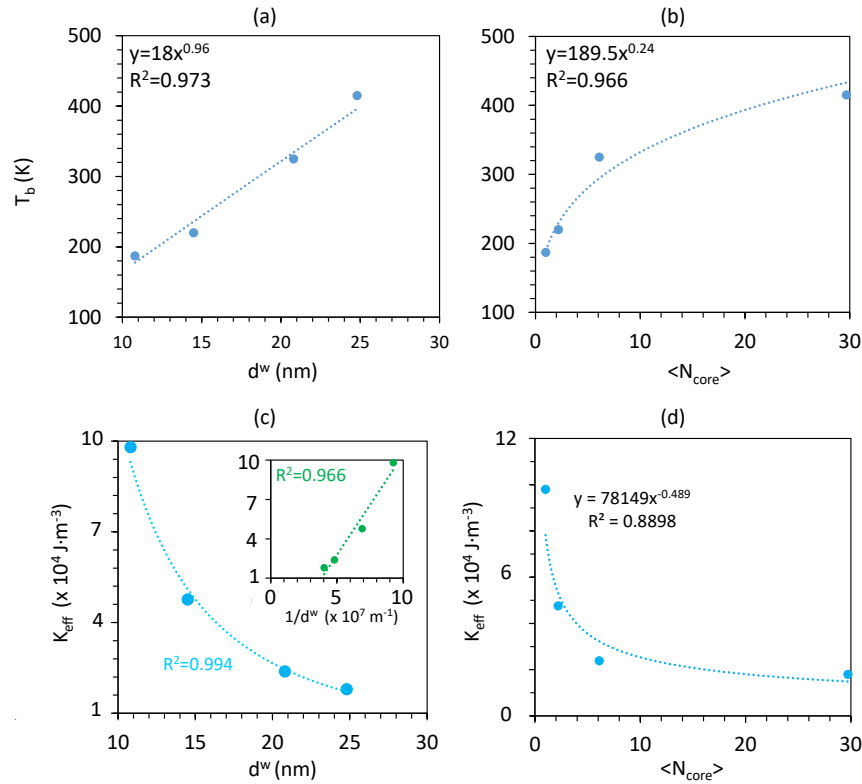


Figure 4. Scaling law determination between magnetic parameters from ZFC-FC curves and structural parameters: Plots of (a,b) blocking temperature $\langle T_B \rangle$ and (c,d) effective anisotropy K_{eff} versus (a, c) weight-average diameter from the Langevin fit of the VSM curves d^w and (b, d) number $\langle N_{\text{core}} \rangle$ of cores. The inset in (c) shows K_{eff} vs. $1/d^w$.

Magnetic Properties (Part 3): AC Magnetization Curves of IONPs

During the past decades, many studies have shown the great impact of the size and size distribution as well as of the particle crystallinity and chemical composition on the heating efficiency of IONPs.^{[33],[76],[77]} In terms of theoretical predictions, the so-called Linear Response Theory (LRT)^[78] and the Stoner-Wohlfarth (SW) model^[79] demonstrated correlation between the field amplitude, the intrinsic properties of the NP and their heating power. Both models predict a sharp maximum of the heating power for a well-defined diameter at certain field conditions followed by an abrupt decrease when the mean particle size differs only by a few nanometers with respect to the ideal size.^[61] This size optimum has been observed experimentally for iron oxide or pristine iron NPs with a nearly spherical,^{[80],[41],[81]} or a cubic morphology^{[82],[83]}. Concerning truly multicore IONFs or simply clustered IONPs (*i.e.* without sintering, being polycrystalline),^[12] the magnetic behavior appears in all cases to be governed by intra-particle characteristics *i.e.* intra-particle dipolar interactions and surface spin disorder (aka spin-canting) which both impact the magnetic anisotropy energy, as illustrated in several studies. For instance, Blanco-Andujar *et al.* reported that magnetic interactions alongside with the number, size and spatial arrangement of the cores directly affect the final heating properties of IONFs obtained by a microwave synthesis in the presence of citrate ligands.^[84] Similarly, Storozhuk *et al.* reported an exceptional enhancement of the heating power of IONPs when increasing their size *via* a seeded-growth strategy. However, previous studies by Lévy *et al.* had shown that simple IONP size growth without reaching a monocrystalline state is not sufficient to raise the heating properties.^[61] The positive impact of the size increase on the heating rate necessitates that the enhanced magnetic exchange couplings within the cores overrides the negative effect of structural defects and misalignments that inevitably arise between the cores during the seeded growth step of the IONPs.^[85] Interestingly, defects have been shown to be beneficial to increase the magnetic anisotropy energy (originating from shape or surface), eventually improving the heating properties,^[64] which explains the higher SAR observed for magnetic nano-cubes as compared to nano-spheres of same volume.^[82] In all cases, the balance between inter-core magnetic dipolar interactions *versus* exchange energy between magnetic domains can give rise to the appearance of a size optimum exhibiting exceptional heating properties, as reported for 50 nm iron oxide nanoclusters exhibiting “superferrimagnetic” behavior.^[19]

In the present work, the heating efficiency of the IONPs was evaluated by AC magnetometry experiments. This method was preferred when compared to classical calorimetry experiments to avoid errors arising from non-adiabatic condition (thermal losses towards the environment) and to study several AC magnetic field conditions (amplitude and frequency) within reasonable experimental time. In this case, an alternating magnetic field (AMF) is applied *via* a commercial resonant circuit (NanoTech Solutions, Madrid, Spain), inducing the oscillation of magnetic moments of the NPs to follow the applied field, yet with a phase lag. This phase lag manifests itself by

the opening of a dynamic hysteresis loop when plotting the instantaneous IONP magnetization M_t vs. the applied field H_t at time t recorded at a given frequency f and alternating magnetic field amplitude H_{\max} . In this case, the energy dissipated into heat by the NPs corresponds to the area A of the recorded hysteresis loop during one AMF cycle $T=2\pi/f$. The specific absorption rate (SAR) is defined by the heat loss power normalized by the NPs' mass following the equation below:

$$\text{SAR} = \frac{\pi f}{c} A \quad \text{with} \quad A = \oint_{-H_{\max}}^{+H_{\max}} M_t dH_t \quad \text{Eq. (9)}$$

where M_t is the instantaneous magnetization ($\text{A}\cdot\text{m}^{-1}$) at time t , H_t the field intensity ($\text{A}\cdot\text{m}^{-1}$) at time t , f (Hz) the applied magnetic field frequency and c ($\text{kg}\cdot\text{m}^{-3}$) the nanoparticle weight concentration of iron oxide in the dispersing medium (SAR is most often expressed in $\text{W}\cdot\text{g}^{-1}$ iron oxide or iron rather than $\text{W}\cdot\text{kg}^{-1}$).^{[41],[39],[79]}

The larger the area A of the hysteresis loops, the larger the energy dissipated by the IONPs per AMF cycle and hence the SAR.^[31] Curves showing the hysteresis loops and plots of SAR vs. H_{\max} of NF1, 4 and 6 at different probed frequencies are gathered on **Figure 5**. The hysteresis loops as well as A vs. H_{\max} and SAR vs. H_{\max} for all set of NPs are found in SI (**Figures S11 to S17**). Evolution of the hysteresis cycle shape with the size of the IONPs is observed, going from narrow (sample NF1) towards larger, more “open” and “square” loops (sample NF4 and 6) as seen in **Figure 5**. A power law fitting with an exponent varying from 1.5 to 2 of SAR vs. H_{\max} curves is observed for all the set of NPs. This approximate quadratic dependence $\text{SAR} \propto H_{\max}^2$, as described by the Linear-Response Theory (LRT) also called “Rosensweig’s model”, indicates a superparamagnetic behavior of the synthesized IONPs batches.^[86] Please note that the SAR vs. H_{\max} curves of NF6 follows pure quadratic dependence with an exponent of nearly 2, at all tested frequencies, in perfect agreement with the LRT originally built for purely superparamagnetic systems, although the same trend was found even for NF7 that exhibits a small hysteresis of DC magnetization at RT. On the other hand, for all the set of NFs, the plots of hysteresis cycle area A vs. H_{\max} at each tested frequency collapse onto a unique master curve as shown in **Figures S11-17**. Area values as well as SAR of IONPs at two field conditions (280 kHz, for 12 and 24 $\text{kA}\cdot\text{m}^{-1}$) are gathered in **Table 3**. Until now, the highest area A of dynamic hysteresis cycle reported in literature by Mehdaoui *et al.* is 11.2 $\text{mJ}\cdot\text{g}^{-1}$ for pristine Fe nanocubes of 13.7 nm size.^[41] For the samples here made of iron oxide (that has advantage of chemical stability and biocompatibility compared to pristine iron), hysteresis area giving the loss per cycle reaches a value as high as $A=2.70 \text{ mJ}\cdot\text{g}^{-1}$ for sample NF6 of 28.7 nm average diameter at $f=280 \text{ kHz}$ and $H_{\max}=24 \text{ kA}\cdot\text{m}^{-1}$. This value is 1.5 times higher than the A value reported by Marciello *et al.* ($A=1.83 \text{ mJ}\cdot\text{g}^{-1}$ at $f=70 \text{ kHz}$ and $H_{\max}=35 \text{ kA}\cdot\text{m}^{-1}$) in their work of IONPs synthesis optimization for magnetic hyperthermia.^[87]

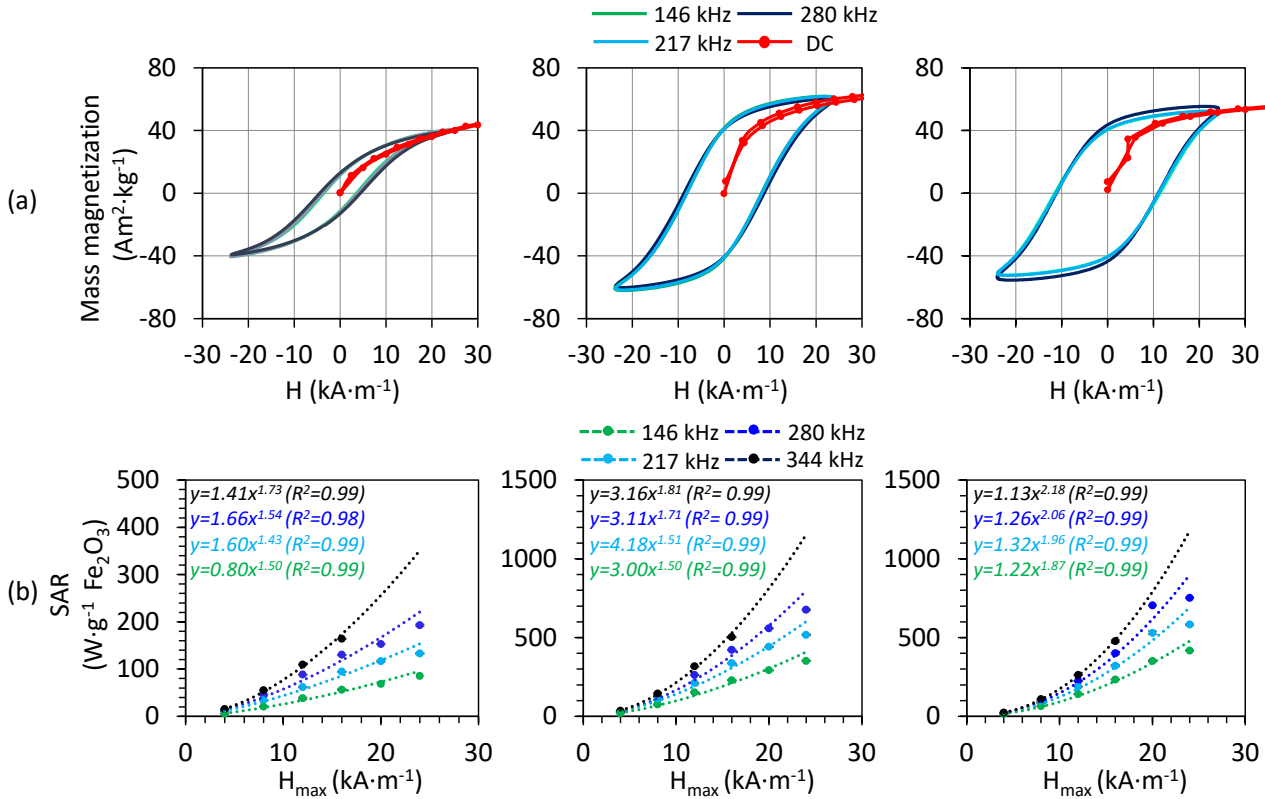


Figure 5. From left to right: Plots of (a) hysteresis loops at $f=146, 217$ and 280 kHz superimposed with the DC curve at low applied H and (b) SAR vs. H_{\max} fitted with a power law of samples NF1, NF4 and NF6 respectively.

The SAR dependency plots on the external (TEM), the crystal and the magnetic monodomain diameters (d_{TEM} , d_{XRD} , d^w respectively) as well as $\langle N_{\text{core}} \rangle$ are gathered in **Figure 6** for four frequencies (146, 217, 280, 344 kHz) at $H_{\max} = 12$ kA·m⁻¹ (right row) and 24 kA·m⁻¹ (left row) field amplitudes. As expected, the SAR values rise when increasing the AMF frequency or amplitude. When comparing the batches at high field amplitude ($H_{\max} > 16$ kA·m⁻¹), the SAR increases monotonously with outer size d_{TEM} , crystalline size d_{XRD} and magnetic domain size d^w for all probed frequencies as shown in **Figure 6 (a-c)** for $H_{\max} = 24$ kA·m⁻¹ and **S18-S20** for $H_{\max} = 20$ kA·m⁻¹. More precisely, SAR increases progressively with d_{TEM} , d_{XRD} or d^w by following power laws of respective exponents $a_{\text{TEM}} \sim 1.5-1.8$, $a_{\text{XRD}} \sim 1.6-1.9$ and $a_{\text{VSM}} \sim 1.5-1.8$ when f varies from 146 to 280 kHz and for $H_{\max} > 16$ kA·m⁻¹. Furthermore, the best fit is obtained (*i.e.* with coefficients of determination R^2 the closest to 1) when plotting SAR vs. d_{XRD} , with SAR continuously increasing with the crystal size for $H_{\max} > 16$ kA·m⁻¹.

Samples	$H_{\max}=24 \text{ kA}\cdot\text{m}^{-1}$		$H_{\max}=12 \text{ kA}\cdot\text{m}^{-1}$	
	$A \text{ (mJ}\cdot\text{kg}^{-1})$	$\text{SAR (W}\cdot\text{g}^{-1})$	$A \text{ (mJ}\cdot\text{kg}^{-1})$	$\text{SAR (W}\cdot\text{g}^{-1})$
NF1	693.2 ± 3.0	192.7 ± 0.8	316.9 ± 1.3	88.2 ± 0.3
NF2	1320 ± 14	430.0 ± 3.3	679.1 ± 10.1	189.1 ± 2.7
NF3	2266 ± 22	639.0 ± 6.2	923.8 ± 10.9	257.2 ± 3.0
NF4	2430 ± 17	676.2 ± 4.7	944.3 ± 2.8	262.8 ± 0.7
NF5	1700 ± 8	473.2 ± 2.1	789.1 ± 5.6	219.7 ± 1.5
NF6	2700 ± 17	751.3 ± 4.7	804.7 ± 1.9	224.2 ± 0.5
NF7	2076 ± 29	578.1 ± 8.20	695.9 ± 6.8	193.7 ± 1.9

Table 3. Values of hysteresis loop area A and SAR expressed in $\text{mJ}\cdot\text{kg}^{-1}$ and $\text{W}\cdot\text{g}^{-1}$ Fe_2O_3 respectively, recorded by AC magnetometry at 280 kHz for $H_{\max} = 12$ and $24 \text{ kA}\cdot\text{m}^{-1}$ for all the set of IONPs.

On the other hand, when analyzing the plot of SAR vs. d_{TEM} , it reaches a maximum of $751 \text{ W}\cdot\text{g}^{-1} \text{ Fe}_2\text{O}_3$ at $d_{\text{TEM}}=28.7$ nm and then slightly decreases down to $575 \text{ W}\cdot\text{g}^{-1} \text{ Fe}_2\text{O}_3$ at $d=29.3$ nm (sample NF7) at 280 kHz and $24 \text{ kA}\cdot\text{m}^{-1}$. The slight decrease of SAR is observed for each probed frequency and can be ascribed to loss of the superparamagnetic properties at $d\sim 30$ nm when the NPs start exhibiting ferromagnetic behavior as shown previously from the small hysteresis appearing on the DC magnetization curves of NF7 (**Figure 3(c)**). Another explanation can be the lower crystalline domain size d_{XRD} of sample NF7 as compared to NF6. On the other hand, when comparing the three analogous samples NF3, NF4, NF5, synthesized using identical polyol conditions, a slight decrease of SAR was observed from 639 and $676 \text{ W}\cdot\text{g}^{-1} \text{ Fe}_2\text{O}_3$ (NF3 and NF4 respectively) to $473 \text{ W}\cdot\text{g}^{-1} \text{ Fe}_2\text{O}_3$ for NF5 at 280 kHz and $24 \text{ kA}\cdot\text{m}^{-1}$. It is worth noticing that among the three analogous samples, NF5 has the lowest crystalline and magnetic domain sizes, a sign of more disordered state which undoubtedly affects its heating properties.

Interestingly, the nearly parabolic increase of SAR vs. d_{TEM} , d_{XRD} and d^w is lost at lower field amplitudes at almost all probed frequencies (R^2 too low when fitting with a power law, the dashed lines in **Figure 6 (b), (d) and (f)** for $12 \text{ kA}\cdot\text{m}^{-1}$ being given only as guides for the eye), accompanied by decrease of spread of SAR values among the samples. Furthermore, depending on the probed frequency, the appearance of a new size optimum for which SAR reaches a maximal value at low field amplitude was noticed. For instance, at $f=146\text{-}344$ kHz, the optimal size is $d_{\text{TEM}}=22.2$ nm ($d_{\text{XRD}}=20.8$ nm; $d^w=19.5$ nm) corresponding to sample NF4 for $H_{\max} = 12 \text{ kA}\cdot\text{m}^{-1}$ as shown in **Figure 6 (b), (d) and (f)** and for $H_{\max} = 16 \text{ kA}\cdot\text{m}^{-1}$ as shown in **Figure S18-20 (b)**.

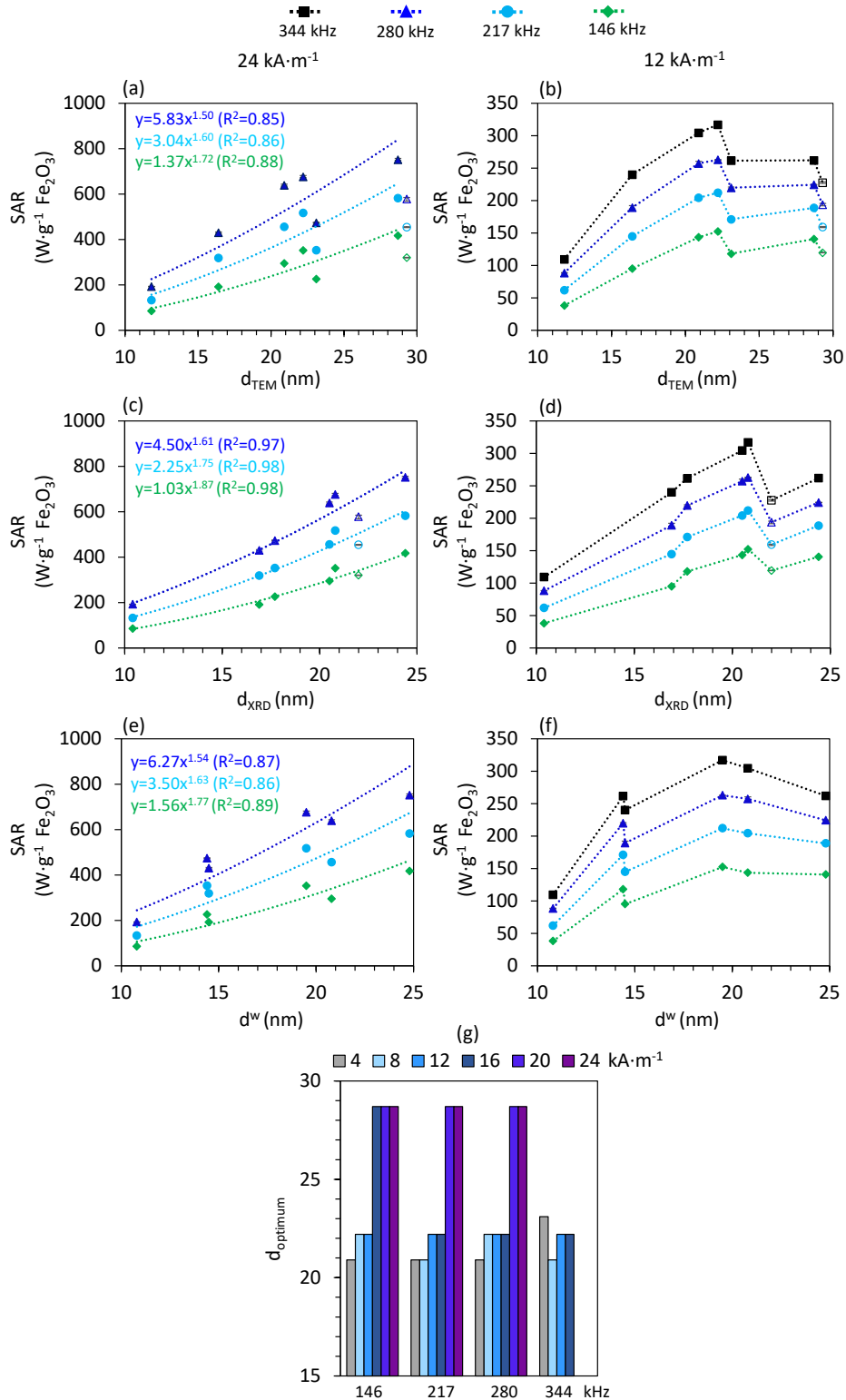


Figure 6. (a-b) SAR variation with outer size (d_{TEM}), (c-d) crystalline size (d_{XRD}) or (e-f) magnetic domain size (d^w) probed at $H_{\text{max}}=24 \text{ kA}\cdot\text{m}^{-1}$ (left column) and $12 \text{ kA}\cdot\text{m}^{-1}$ (right column). Please note the linearity loss as well as the appearance of a new SAR maximum for $d_{\text{opt}}=22.4 \text{ nm}$. (g) Variation of d_{opt} with the applied field amplitude H_{max} at

all probed frequencies. Please note that the unfilled datapoints correspond to sample NF7, presenting ferromagnetic contribution.

Similarly, for $f=217$ and 344 kHz, the optimum size shifts from NF4 ($d_{\text{TEM}}=22.2$ nm; $d_{\text{XRD}}=20.8$ nm; $d^w=19.3$ nm) at $H_{\text{max}}=12-16$ kA·m⁻¹ to NF3 ($d_{\text{TEM}}=20.9$; $d_{\text{XRD}}=20.5$ nm; $d^w=19.9$ nm) at $H_{\text{max}}=8$ kA·m⁻¹ (**Figure S18-20 (c)**) and then NF5 ($d_{\text{TEM}}=23.1$ nm; $d_{\text{XRD}}=17.7$ nm; $d^w=14.4$ nm) at 4 kA·m⁻¹ (**Figure S18-20 (d)**) respectively. **Figure 6 (g)** represents the evolution of the optimum size (d_{opt}) taken from the SAR vs. d_{TEM} variation curves, for different AMF amplitudes H_{max} and frequencies f . A general trend is observed with d_{opt} shifting towards higher values when increasing the applied field amplitude H_{max} . The increase of d_{opt} with the applied AMF amplitude has recently been reported by the theoretical study of Engelmann *et al.*, where they used Monte Carlo (MC) simulations to predict the heating power of iron oxide NPs.^{[42],[43]} The SAR dependence with the size of the NPs, as predicted by these MC simulations follows tendencies that are analogous to our experimental results. For instance, when considering $K_{\text{eff}}=11$ kJ·m⁻³ as effective anisotropy constant for MC simulations, Engelmann *et al.* found a Gaussian-like dependency of the SAR vs. NP diameter curve, for both $H_{\text{max}}=16$ and 5 kA·m⁻¹ at 176 kHz. In addition, these authors report a shift of the d_{opt} from 18 to 22 nm when rising the field H_{max} from 5 to 16 kA·m⁻¹ at 176 kHz. Their MC simulations match quite well with our results, as we experimentally observe curves displaying maxima for $H<16$ kA·m⁻¹ as well as a shift of d_{opt} from 20.9 to 22.2 nm when the field amplitude increases from 4 to 12 and 16 kA·m⁻¹ at 146 kHz as shown in **Figure 6 (g)** and **S18 (c-d)** for 146 kHz (green curve). There is also similarity between the range of SAR values predicted by the MC simulations and the experimental values of the present study. On the other hand, Mehdaoui *et al.* attributed the shift of d_{opt} size of pristine Fe nanocubes when increasing the magnetic field as a natural consequence of theory derived from the 2-state Stoner-Wohlfarth model where the maximum area A of hysteresis loop is obtained for an optimal coercive field, situated slightly below H_{max} and related to the particle volume V and applied magnetic field amplitude H_{max} as follows^[41]:

$$\mu_0 H_{\text{max}} \gtrsim \mu_0 H_c = 0.48 \mu_0 H_K (1 - k^{0.8}) \quad \text{Eq. (10)}$$

H_K being the anisotropy field ($H_K = \frac{2K_{\text{eff}}}{\mu_0 M_s}$) and $k = \left(\frac{k_B T}{K_{\text{eff}} V} \right) \ln \left(\frac{k_B T}{4 \mu_0 M_s H_{\text{max}} \tau_0 V} \right)$, τ_0 is the frequency factor of Néel's relaxation time.

Optimum conditions for maximal A happen when H_c is close to H_{max} . Thus, for an increasing field, optimal conditions are created for larger H_c , which is obtained at higher particle volume V (higher V decreases k). This explains the increase of d_{opt} at higher field amplitudes, for given frequency, within the Stoner Wohlfarth model.

Inspired by the recent work of Bertuit *et al.*, we also studied the evolution of SAR with the number of cores composing the NFs. The mean core size remaining similar over all the set of NFs enables us to compare how $\langle N_{\text{core}} \rangle$

affects the heating efficiency among the samples. The curves of SAR vs. $\langle N_{\text{core}} \rangle$ are shown in **Figure 7 (a-b)** for $H_{\text{max}}=24$ and $12 \text{ kA}\cdot\text{m}^{-1}$ as well as **Figure S21 (a-d)** for all the other probed AMF conditions. As shown in **Figure 7 (a)**, the SAR starts to increase linearly with $\langle N_{\text{core}} \rangle$ but passed a local peak near $\langle N_{\text{core}} \rangle = 5-6$, the SAR starts to go down for larger $\langle N_{\text{core}} \rangle$ values up to ~ 10 , and then it is only at much higher value $\langle N_{\text{core}} \rangle \sim 30$ that the SAR starts to rise again, for all probed frequencies. Under these conditions, the highest SAR value is systematically obtained for the highest $\langle N_{\text{core}} \rangle \sim 30$ corresponding to NF6. These results correspond well with the report of Bertuit *et al.* where the highest SAR was obtained for the largest $\langle N_{\text{core}} \rangle = 23$ at $H_{\text{max}} = 14.3 \text{ kA}\cdot\text{m}^{-1}$ and $f = 471 \text{ kHz}$. But contrary to our result, their evolution of SAR with $\langle N_{\text{core}} \rangle$ at $H_{\text{max}} = 14.3 \text{ kA}\cdot\text{m}^{-1}$ and $f = 471 \text{ kHz}$ remained perfectly linear even at high $\langle N_{\text{core}} \rangle$.^[35] This linear correlation between SAR and $\langle N_{\text{core}} \rangle$ was attributed to the exchange couplings between the cores that are enhanced at high $\langle N_{\text{core}} \rangle$ and as consequence improve the heating power of the NPs. In the present report, the evolution of SAR with $\langle N_{\text{core}} \rangle$ was examined at various frequencies and field amplitudes. We observe that when the field amplitude decreased $H_{\text{max}} < 16 \text{ kA}\cdot\text{m}^{-1}$, the plot of SAR vs. $\langle N_{\text{core}} \rangle$ increases linearly up until reaching a new SAR maximum for $\langle N_{\text{core}} \rangle = 5$ corresponding to NF4 sample and then slightly decreasing at larger $\langle N_{\text{core}} \rangle$. This tendency was observed at all probed frequencies for $H_{\text{max}} = 4-16 \text{ kA}\cdot\text{m}^{-1}$ (**Figure 7(b)**) and **Figure S21 (c-d)**. Similarly, to d_{opt} , the optimum $\langle N_{\text{core}} \rangle$, corresponding to the highest SAR value, shifts towards higher values when increasing the magnetic field amplitude H_{max} .

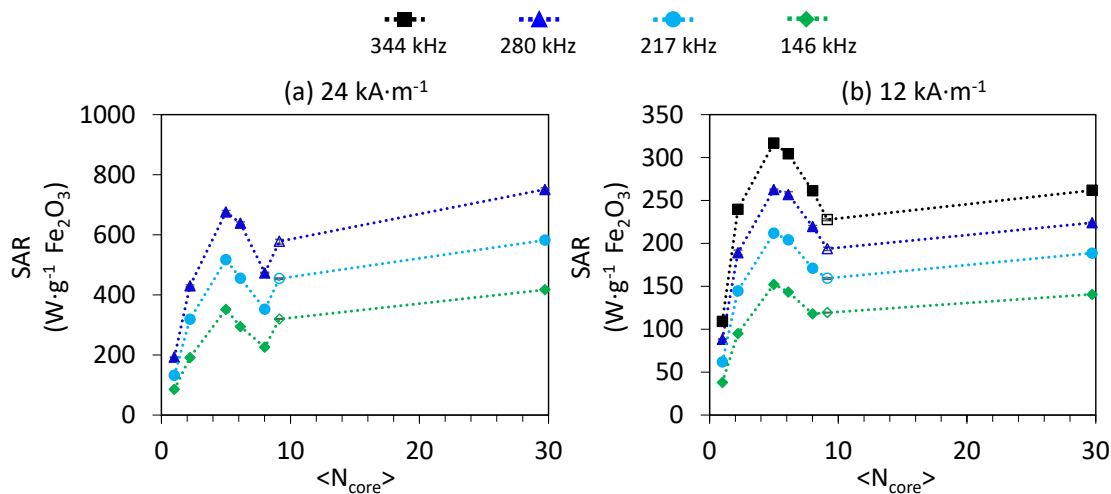


Figure 7. SAR evolution with $\langle N_{\text{core}} \rangle$ for four frequencies at (a) $H_{\text{max}}=12$ and (b) $H_{\text{max}}=24 \text{ kA}\cdot\text{m}^{-1}$.

In addition to SAR, the evolution of the hysteresis loop “squareness” with $\langle N_{\text{core}} \rangle$ of the NFs was also investigated. The “raw” plots of the hysteresis loops superimposed for all samples sorted in the order of increasing $\langle N_{\text{core}} \rangle$ are given in **Figure 8 (a)** for $H_{\text{max}}=24 \text{ kA}\cdot\text{m}^{-1}$ at $f=280 \text{ kHz}$, while plots of raw and normalized curves of hysteresis loops are found in **Figure S22** for $H_{\text{max}}=4, 12$, and $16 \text{ kA}\cdot\text{m}^{-1}$ at $f=280 \text{ kHz}$. As it can be seen, although the overall shape

of the hysteresis cycle still is similar within the different IONPs, the loop “opens up” towards a more “square-like” shape when increasing $\langle N_{core} \rangle$. Please notice how the sample NF6 which owns the highest $\langle N_{core} \rangle$ systematically has the largest coercive fields H_c , hence the most “open” loop at all applied fields, as illustrated in the normalized hysteresis plots (see **Figure S22 (b), (d) and (f)**).

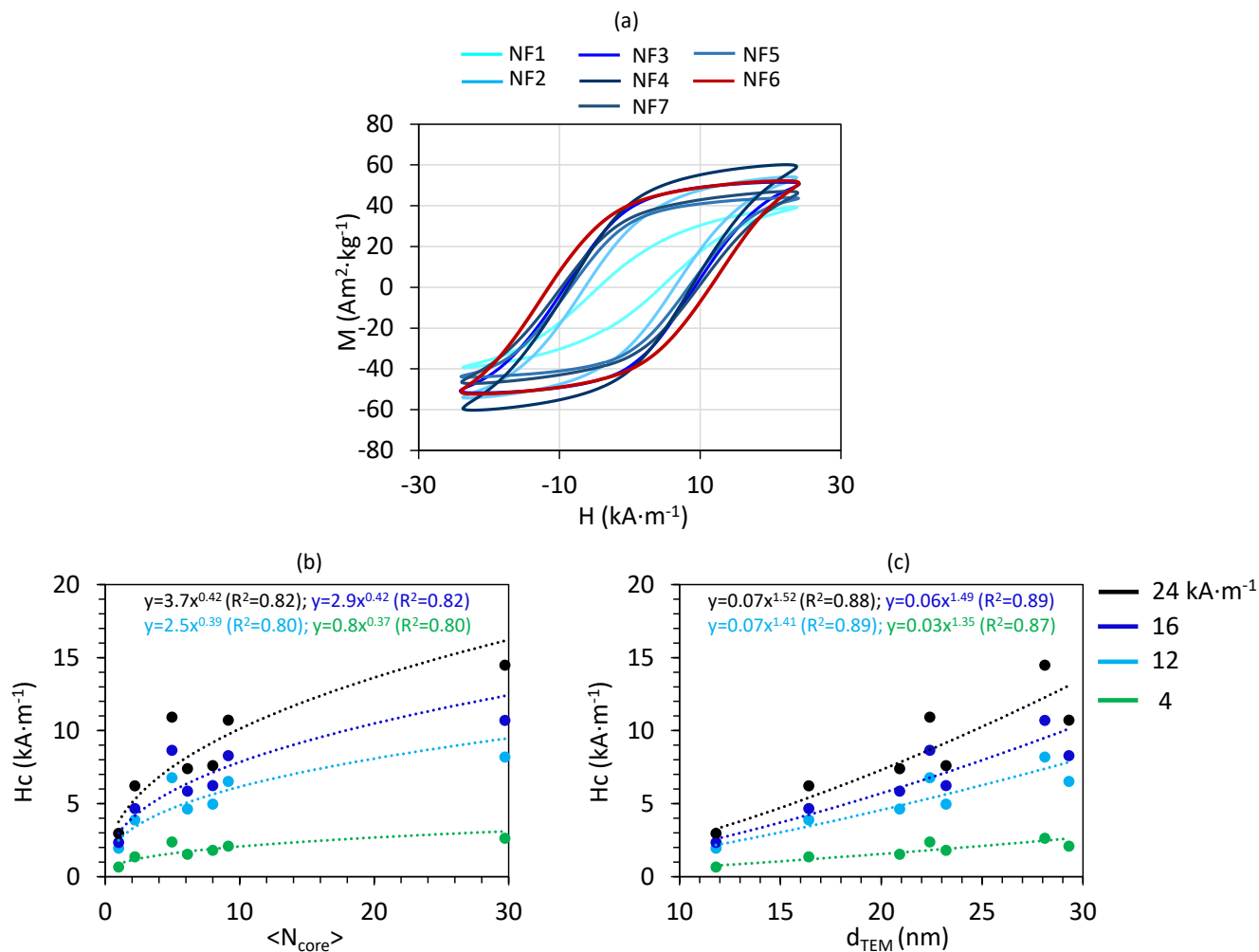


Figure 8. (a) Superimposed hysteresis cycles of NF1-7 at 24 kA·m⁻¹ and 280 kHz. (b) and (c) Evolution of the coercive field H_c of IONPs vs. the mean core number $\langle N_{core} \rangle$ and the diameter d_{TEM} respectively. At all applied fields, the sample having the largest number of grains (NF6) exhibits the highest H_c .

To better illustrate this tendency, the graphs of H_c vs. $\langle N_{core} \rangle$ and H_c vs. d_{TEM} were plotted on **Figure 8 (b-c)**. It is noticeable that the coercive field follows a power law with d_{TEM} of exponent ~ 1.4 - 1.5 . On the other hand, H_c increases with $\langle N_{core} \rangle$ following a power law of exponent ~ 0.40 , therefore the highest H_c is reached for the highest $\langle N_{core} \rangle$ (sample NF6) at all applied fields. The increase of H_c with the particle diameter and $\langle N_{core} \rangle$ is related to an overall increase of the anisotropy barrier when increasing the size, as well as interactions between cores that rise

at larger $\langle N_{\text{core}} \rangle$ values. Therefore, a higher applied field is needed to reverse the magnetization of larger NPs with enhanced intra-particle interactions. Contrary to the variation of SAR plotted vs. $\langle N_{\text{core}} \rangle$ that presents a maximum, the H_c vs. $\langle N_{\text{core}} \rangle$ and H_c vs. d_{TEM} graphs display the same monotonous increase tendencies under all conditions of the applied magnetic field.

Discussion

In this paper, the relationship between structural and magnetic properties of IONPs produced *via* a simple polyol route were investigated. IONPs within the size range of 10 to 30 nm were prepared by slightly modifying the original polyol conditions firstly introduced by Caruntu *et al.* We noticed that when inducing faster nucleation of NPs by either adding H₂O or increasing the content of DEG in the polyol medium, a decrease in the overall size was witnessed and a morphology change of the NPs from multi to moncore NPs were induced. However, when using classical polyol conditions, the synthesized IONPs exhibited both morphologies – mono and multicore – the latter being the predominant morphology. SAED and XRPD diffraction patterns coincide well with the tabulated peaks for magnetite and maghemite. The cell parameter deduced from XRPD pattern refinement are found to be in between magnetite and maghemite for all our samples. According to a series of reports by Tourinho, Depeyrot *et coll*,^[88] the oxidation step of metal ferrite NPs by a boiling solution of Fe(NO₃)₃ has a much size-dependent kinetics. Therefore, this treatment is likely incomplete, as indicated by several clues in the present work evidencing the presence of magnetite within the NPs, starting by their visible-NIR absorbance spectrum where the NIR band, corresponding to IVCT of magnetite, increased with the size of the NP, indicating a higher proportion of magnetite for the largest samples. The presence of magnetite was also seen on the ZFC/FC curves through the Verwey transition occurring at T \approx 110-170 K on the largest tested samples (**Figure S9** for NF3 and **Figure S10** for NF6). Besides the composition, structural defects are known to affect the magnetic properties of IONPs. Thus, structural defects were evidenced by performing a FFT treatment on the HR-TEM images. A difference was seen amongst the sample series: NF1 and NF2 appeared rich in spherical moncore NPs with little to no defects among the studied planes whereas NF3-NF6 were dominated by multicore NPs presenting zones with visible misalignments along (220), (311), and (211) planes, as shown in **Figure S5**. The presence of crystalline defects within the multicore NPs was confirmed also by fluorimetry, where intense emission was observed for multicore NPs, with the luminescence intensity increasing with their size, mean $\langle N_{\text{core}} \rangle$ number and notably with the outer surface area ($\propto d_{\text{TEM}}^2$), as a result of higher defect concentration.^[35] This atomic disorder directly also influences the specific saturation magnetization of the NPs: their M_s value decreases with the multicore NP proportion as well as the number $\langle N_{\text{core}} \rangle$, despite the overall size increase of the IONPs, due to the loss of the crystal integrity with the presence of defects, and the surface disorder as well. Furthermore, when comparing samples NF3, NF4 and NF5

synthesized under identical conditions and with similar d_{TEM} and M_s , NF5 displays the lowest heating efficiency amongst them (except at lowest AMF amplitudes). The main difference within these samples is the mean magnetic diameter, which for NF5 is quite low when compared to its overall diameter ($d_{\text{TEM}}=23.1$ nm, $d^{\text{M}}=14.2$ nm) and close to that of NF2 ($d_{\text{TEM}}=16.4$ nm, $d^{\text{M}}=14.5$ nm). With distinct outer diameters but remarkably similar magnetic domain size, these two samples have similar heating efficiencies under all probed AMF conditions, despite the higher $\langle N_{\text{core}} \rangle$ of NF5. In this case, we relate the lower heating efficiency of NF5 compared to its analogous samples NF3 and NF4, as a direct consequence of a lower magneto-crystalline energy barrier ΔE_{ani} , due to its smaller magnetic volume. This also explains why the samples NF2 and NF5 with distinct core diameters, but similar magnetic domain and crystal sizes, lead in the end to similar heating properties. In addition, NF6 and NF7 samples, which are also synthesized under identical polyol conditions, do not have the same properties despite their close diameters (28.1 nm for NF6 and 29.3 nm for NF7). For instance, NF7 exhibits a lower crystal size, $\langle N_{\text{core}} \rangle$ and a ferromagnetic behavior, when compared to NF6, all in detriment to its heating properties. The comparison between these two sets of analogous NPs clearly demonstrates that the classic polyol route offers a good reproducibility of NPs in terms of overall diameter and morphology *i.e.* mono or multicore, but that it lacks control on the detailed structural features that directly affect the heating efficiency of IONPs (*i.e.* crystal and magnetic size, $\langle N_{\text{core}} \rangle$, size-distribution etc.). The low yield, the high energy consuming synthesis alongside the lack of control of NPs' intrinsic properties affecting their SAR represent the main drawbacks of the polyol route. Solutions to these issues in the near future may involve the use of novel polyol reactors *i.e.*, milli-fluidic continuous flow reactors, recently reported by Bertuit et al,^[89] which allow for a better control of the final physicochemical properties of IONFs as well as their large-scale production.

Besides structural parameters, we also bring proof that the heating efficiency of IONPs is tightly related to the applied magnetic field conditions as well. Firstly, the SAR variation as H_{max}^2 observed for all IONPs, evaluated at various AMF conditions, is predicted by the LRT theory for superparamagnetic NPs. Secondly, the simultaneous dependence of SAR with IONP size and magnetic field conditions can be summarized by considering two regimes:

- (1) High field amplitude regime for $H \geq 20$ kA·m⁻¹ where the highest SAR was found for the largest NF6 batch (TEM diameter of ~29 nm) also corresponding to the largest crystalline size (~24 nm), magnetic domain size (~25 nm) and mean $\langle N_{\text{core}} \rangle$ number (~30);
- (2) Low field amplitude regime $H_{\text{max}} \leq 16$ kA·m⁻¹ where the optimal TEM diameter d_{opt} shifts to ~22 nm ($H_{\text{max}} = 12-16$ kA·m⁻¹) or ~21 nm ($H_{\text{max}} = 8$ kA·m⁻¹).

Furthermore, the evolution of SAR with $\langle N_{\text{core}} \rangle$ is also dependent on the field conditions. Under high field amplitude regime, the highest SAR corresponds to sample NF6 of ~29 nm diameter with the highest $\langle N_{\text{core}} \rangle \sim 30$,

which can be explained as a consequence of its high magnetic domain size (close to its crystal size) as well as enhanced exchange interactions at high $\langle N_{\text{core}} \rangle$ as recently reported by Bertuit *et al.*^[35] In our study, we clearly demonstrate that the evolution of SAR with $\langle N_{\text{core}} \rangle$ deviates from linear trend when decreasing the field amplitude H_{max} , showing an intermediate value of $\langle N_{\text{core}} \rangle \sim 5$ maximizing the SAR. This finding completes the result of Bertuit *et al.* where the SAR linearity with $\langle N_{\text{core}} \rangle$ was demonstrated only under one AMF condition *i.e.* $H_{\text{max}}=14 \text{ kA}\cdot\text{m}^{-1}$ and $f=471 \text{ kHz}$.

Revisiting the Stoner-Wohlfarth 2-state model of uniaxial anisotropic particles in the ferromagnetic regime to apply it for AC hysteresis prediction, Mehdaoui *et al.* reported results analogous to ours for pristine Fe nanocubes. Like us, they experimentally observed an increase of the coercive field with the size of the NPs as well as the increase of d_{opt} diameter maximizing the SAR with the amplitude of the magnetic field.^[41] In the case of multicore nanoflowers, the coercive field H_c also increased with the mean number of cores $\langle N_{\text{core}} \rangle$ under all applied AMF conditions. In other works by Engelmann *et al.*,^{[33],[43],[42]} the same trends were found by Monte Carlo simulations for SAR prediction on superparamagnetic spherical iron oxide more similar to our NPs:

- (1) either sigmoidal monotonous increase of SAR with size for high field amplitudes H_{max} , or an increase of SAR followed by a decrease for smaller field amplitudes H_{max} , giving rise to an optimal diameter d_{opt} ;
- (2) a shift of d_{opt} towards larger values when increasing field amplitude H_{max} .

This kind of SAR dependence with the magnetic field and size was explained by taking in account the anisotropy field of the NPs, H_K . Due to the high anisotropy of the NPs studied in this work, the applied field amplitude remains negligible compared to H_K , signifying that the heating contribution arises mainly from the superparamagnetic behavior. Thus, increasing the particle diameter d leads to the suppression of thermal activation due to the particle moment blocking, and as a result SAR decreases for diameters above the optimal value d_{opt} .^[90]

Furthermore, like LRT, the MC simulations of the studies mentioned above predict a $\text{SAR} \propto H^2$ variation for $H \ll H_K$, which is observed in the case of all our IONPs (see calculated values of H_K in Table 2). The increase of the d_{opt} value with the magnetic field is also predicted within the Monte-Carlo simulations, although clear physical explanation of this phenomenon was not found and up to now it has been explained through the Stoner Wohlfarth model.^[41] The results presented in this report suggest that the choice of the IONPs for biomedical applications should be adapted with the used magnetic field conditions. For instance, in order to respect the clinical “Brezovitch’s limit” ($H \times f < 5 \times 10^9 \text{ A}\cdot\text{m}^{-1}\cdot\text{s}^{-1}$),^[91] two choices for the AMF conditions are possible: low field amplitude and high frequency *i.e.* 280-344 kHz for $H_{\text{max}} \leq 16 \text{ kA}\cdot\text{m}^{-1}$ or high field amplitude and low frequency *i.e.* 146-217 kHz for $H_{\text{max}} > 16 \text{ kA}\cdot\text{m}^{-1}$. Amongst our IONP library, the NF4 of $\sim 22 \text{ nm}$ are the best candidates for the first conditions

whereas the NF6 of ~29 nm are more suitable for the second. In both cases, the maximum SAR reaches the same range of 400-500 W·g⁻¹ Fe₂O₃, which corresponds to suitable values for biomedical applications, where the injected dose of magnetic NPs needs to be minimized.

Conclusion

The extensive investigation of structural, magnetic properties of IONPs, and their impact on the heating efficiency has allowed us to develop a strong foundation which is able to predict the performance of IONPs in a variety of AMF conditions. On the one hand, structural defects present within the multicore morphologies ascribed to their formation pathway (oriented aggregation), lowers the saturation magnetization of the NPs, because of disorder. On the other hand, high levels of structural defects lead to higher magnetic anisotropy energy and higher coercive field H_k , which means more “opened up” hysteresis cycles under AC field excitation. When comparing analogous IONPs, the highest SAR was systematically obtained for the IONPs having a magnetic size close to their crystal and physical diameters. Intra-particle exchange interaction between the cores drives the blocking temperature $\langle T_B \rangle$ towards high values, and thus increases the overall magneto crystalline energy barrier ΔE_{ani} of the NPs. For currently much studied nanoflowers synthesized by the polyol route, our study shows that the mean $\langle N_{core} \rangle$ is not the only parameter affecting their heating efficiency. SAR is indeed a complex property depending simultaneously on structural features (magnetic, crystalline, or overall diameter, $\langle N_{core} \rangle$ number and atomic defects) and on the applied magnetic field conditions. Herein, experimental results clearly demonstrate that the choice of driving field (either at lower amplitude and higher frequency, or the contrary) can select the SAR of NPs between two regimes, either SAR increasing monotonously with diameters or showing a maximum. The optimal diameter d_{opt} also gets shifted towards larger value when the field amplitude H_{max} is increased. Lastly, the heating properties of the IONFs appear to lay in-between the two well-known theoretical models, namely the Linear Response Theory (also called Rosensweig’s model) predicting $SAR \propto H^2$ variation, and the Stoner-Wohlfarth model that was originally built for ferromagnetic NPs. These models give us physical insights why the d_{opt} diameter is shifted towards larger values when the H_{max} amplitude of AMF increases, and why the anisotropy field H_c increases with the size and the number of cores of the nanoflowers. In contrast to theories which have limitation ($d_{NP} < 10$ nm for the LRT, and uniaxial anisotropy for the Stoner-Wohlfarth “two-state model”), numerical MC simulations can extend the predictions of SAR to particles much closer to experimental systems. To our knowledge, there was no previous report of such comprehensive experimental study for multicore iron oxide nanoflowers, agreeing in semi-quantitative way with numerical simulations as those of Engelmann *et al* mentioned before,^{[42],[43]} or very recently by Yoshida and Enpuku who also predicted optimal IONP diameter varying with the excitation AMF conditions.^[92]

Acknowledgments

This study was conducted within the framework of the University of Bordeaux's program "RRI IMPACT" that received France 2030 financial support from the French government and the SIRIC BRIO (AAP 2020 Innovative Equipment for Oncology) enabling to acquire the AC hysteresis magnetometer. It was also partially supported by the grant ANR-22-CE09-0001-01 awarded by the French National Research Agency (ANR).

Supplemental Information

Additional measurements (TEM size histograms, SAED and XRD patterns, absorption and fluorescence spectra, DC magnetization curves, AC hysteresis loops and various other plots) are provided in the supplemental information file that can be downloaded at the publisher's website.

Data Availability

Whenever needed for comparison to other experimental results or theoretical fitting, the raw data of all graphs of this study are freely available on the Zenodo.org public repository (DOI: [10.5281/zenodo.7596848](https://doi.org/10.5281/zenodo.7596848))

References

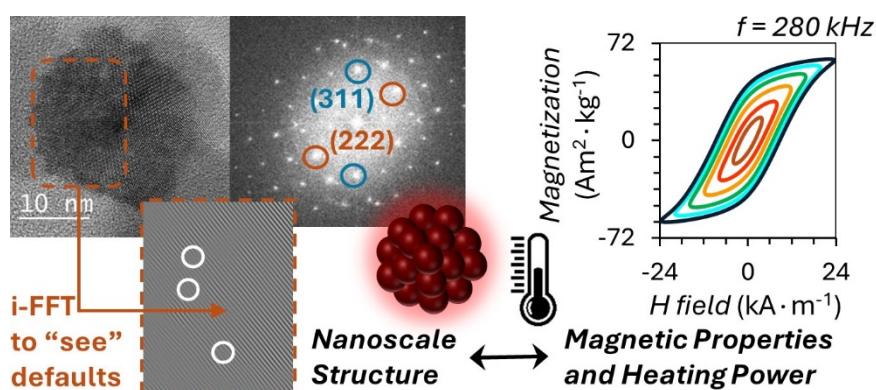
- [1] M. J. Ko, H. Hong, H. Choi, H. Kang, D.-H. Kim, *Adv. NanoBiomed Res.* **2022**, *2*, 2200053.
- [2] Z. Ma, J. Mohapatra, K. Wei, J. P. Liu, S. Sun, *Chem. Rev.* **2023**, *123*, 3904–3943.
- [3] S. M. Dadfar, K. Roemhild, N. I. Drude, S. von Stillfried, R. Knüchel, F. Kiessling, T. Lammers, *Adv. Drug Deliv. Rev.* **2019**, *138*, 302–325.
- [4] T.-J. Yoon, H. Lee, H. Shao, R. Weissleder, *Angew. Chem. Int. Ed.* **2011**, *50*, 4663–4666.
- [5] K. Maier-Hauff, F. Ulrich, D. Nestler, H. Niehoff, P. Wust, B. Thiesen, H. Orawa, V. Budach, A. Jordan, *J. Neurooncol.* **2011**, *103*, 317–324.
- [6] D. Mertz, O. Sandre, S. Begin-Colin, *Biochim. Biophys. Acta BBA - Gen. Subj.* **2017**, *1861*, 1617–1641.
- [7] E. Cazares-Cortes, A. Espinosa, J.-M. Guigner, A. Michel, N. Griffete, C. Wilhelm, C. Ménager, *ACS Appl. Mater. Interfaces* **2017**, *9*, 25775–25788.
- [8] W. Chen, C.-A. Cheng, J. I. Zink, *ACS Nano* **2019**, *13*, 1292–1308.
- [9] B. T. Mai, P. B. Balakrishnan, M. J. Barthel, F. Piccardi, D. Niculaes, F. Marinaro, S. Fernandes, A. Curcio, H. Kakwere, G. Autret, R. Cingolani, F. Gazeau, T. Pellegrino, *ACS Appl. Mater. Interfaces* **2019**, *11*, 5727–5739.
- [10] D. Caruntu, G. Caruntu, Y. Chen, C. J. O'Connor, G. Goloverda, V. L. Kolesnichenko, *Chem. Mater.* **2004**, *16*, 5527–5534.
- [11] J. F. Banfield, S. A. Welch, H. Zhang, T. T. Ebert, R. L. Penn, *Science* **2000**, *289*, 751–754.
- [12] S. Dutz, *IEEE Trans. Magn.* **2016**, *52*, 1–3.
- [13] E. M. Jefremovas, L. Gandarias, I. Rodrigo, L. Marcano, C. Gruttner, J. A. Garcia, E. Garayo, I. Orue, A. Garcia-Prieto, A. Muela, M. L. Fernandez-Gubieda, J. Alonso, L. F. Barquin, *IEEE Access* **2021**, *9*, 99552–99561.
- [14] A. Kostopoulou, A. Lappas, *Nanotechnol. Rev.* **2015**, *4*, 595–624.
- [15] Z. Xiao, L. Zhang, V. L. Colvin, Q. Zhang, G. Bao, *Ind. Eng. Chem. Res.* **2022**, *61*, 7613–7625.
- [16] P. Hugounenq, M. Levy, D. Alloyeau, L. Lartigue, E. Dubois, V. Cabuil, C. Ricolleau, S. Roux, C. Wilhelm, F. Gazeau, R. Bazzi, *J. Phys. Chem. C* **2012**, *116*, 15702–15712.
- [17] D. Maity, S. N. Kale, R. Kaul-Ghanekar, J.-M. Xue, J. Ding, *J. Magn. Magn. Mater.* **2009**, *321*, 3093–3098.
- [18] A. Bunge, A. S. Porav, G. Borodi, T. Radu, A. Pîrnău, C. Berghian-Grosan, R. Turcu, *J. Mater. Sci.* **2019**, *54*, 2853–2875.
- [19] D. Sakellari, K. Brintakis, A. Kostopoulou, E. Myrovali, K. Simeonidis, A. Lappas, M. Angelakeris, *Mater. Sci. Eng. C* **2016**, *58*, 187–193.
- [20] X. Wei, L. Jing, C. Liu, Y. Hou, M. Jiao, M. Gao, *CrystEngComm* **2018**, *20*, 2421–2429.
- [21] L. Mandić, A. Sadžak, I. Erceg, G. Baranović, S. Šegota, *Antioxidants* **2021**, *10*, 1212.
- [22] F. Hu, K. W. MacRenaris, E. A. Waters, E. A. Schultz-Sikma, A. L. Eckermann, T. J. Meade, *Chem. Commun.* **2010**, *46*, 73–75.
- [23] S. Xuan, Y.-X. J. Wang, J. C. Yu, K. Cham-Fai Leung, *Chem. Mater.* **2009**, *21*, 5079–5087.
- [24] R. Hachani, M. Lowdell, M. Birchall, A. Hervault, D. Mertz, S. Begin-Colin, N. T. K. Thanh, *Nanoscale* **2016**, *8*, 3278–3287.
- [25] T. Gaudisson, R. Sayed-Hassan, N. Yaacoub, G. Franceschin, S. Nowak, J.-M. Grenèche, N. Menguy, P. Sainctavit, S. Ammar, *CrystEngComm* **2016**, *18*, 3799–3807.
- [26] F. Spizzo, P. Sgarbossa, E. Sieni, A. Semenzato, F. Dughiero, M. Forzan, R. Bertani, L. Del Bianco, *Nanomaterials* **2017**, *7*, 373.
- [27] B. Zhang, Z. Tu, F. Zhao, J. Wang, *Appl. Surf. Sci.* **2013**, *266*, 375–379.
- [28] A. A. Nikitin, I. V. Shchetinin, N. Yu. Tabachkova, M. A. Soldatov, A. V. Soldatov, N. V. Sviridenkova, E. K. Beloglazkina, A. G. Savchenko, N. D. Fedorova, M. A. Abakumov, A. G. Majouga, *Langmuir* **2018**, *34*, 4640–4650.
- [29] H. Kratz, M. Taupitz, A. A. de Schellenberger, O. Kosch, D. Eberbeck, S. Wagner, L. Trahms, B. Hamm, J. Schnorr, *PLOS ONE* **2018**, *13*, e0190214.

- [30] G. Zoppellaro, A. Kolokithas-Ntoukas, K. Polakova, J. Tucek, R. Zboril, G. Loudos, E. Fragogeorgi, C. Diwoy, K. Tomankova, K. Avgoustakis, D. Kouzoudis, A. Bakandritsos, *Chem. Mater.* **2014**, *26*, 2062–2074.
- [31] G. Hemery, A. C. Keyes, E. Garaio, I. Rodrigo, J. A. Garcia, F. Plazaola, E. Garanger, O. Sandre, *Inorg. Chem.* **2017**, *56*, 8232–8243.
- [32] H. Gavilán, A. Kowalski, D. Heinke, A. Sugunan, J. Sommertune, M. Varón, L. K. Bogart, O. Posth, L. Zeng, D. González-Alonso, C. Balceris, J. Fock, E. Wetterskog, C. Frandsen, N. Gehrke, C. Grüttner, A. Fornara, F. Ludwig, S. Veintemillas-Verdaguer, C. Johansson, M. P. Morales, *Part. Part. Syst. Charact.* **2017**, *34*, 1700094.
- [33] H. Gavilán, K. Simeonidis, E. Myrovali, E. Mazarío, O. Chubykalo-Fesenko, R. Chantrell, L. Balcells, M. Angelakeris, M. P. Morales, D. Serantes, *Nanoscale* **2021**, *13*, 15631–15646.
- [34] E. Bertuit, S. Neveu, A. Abou-Hassan, *Nanomaterials* **2021**, *12*, 119.
- [35] E. Bertuit, E. Benassai, G. Mériguet, J.-M. Greneche, B. Baptiste, S. Neveu, C. Wilhelm, A. Abou-Hassan, *ACS Nano* **2022**, *16*, 271–284.
- [36] K. M. Krishnan, *IEEE Trans. Magn.* **2010**, *46*, 2523–2558.
- [37] Q. A. Pankhurst, N. T. K. Thanh, S. K. Jones, J. Dobson, *J. Phys. Appl. Phys.* **2009**, *42*, 224001.
- [38] E. Garaio, J. M. Collantes, F. Plazaola, J. A. Garcia, I. Castellanos-Rubio, *Meas. Sci. Technol.* **2014**, *25*, 115702.
- [39] E. Garaio, J. M. Collantes, J. A. Garcia, F. Plazaola, S. Mornet, F. Couillaud, O. Sandre, *J. Magn. Magn. Mater.* **2014**, *368*, 432–437.
- [40] C. Guibert, J. Fresnais, V. Peyre, V. Dupuis, *J. Magn. Magn. Mater.* **2017**, *421*, 384–392.
- [41] B. Mehdaoui, A. Meffre, J. Carrey, S. Lachaize, L.-M. Lacroix, M. Gougeon, B. Chaudret, M. Respaud, *Adv. Funct. Mater.* **2011**, *21*, 4573–4581.
- [42] U. M. Engelmann, C. Shasha, I. Slabu, in *Magn. Nanoparticles Hum. Health Med.*, John Wiley & Sons, Ltd, **2021**, pp. 327–354.
- [43] U. M. Engelmann, C. Shasha, E. Teeman, I. Slabu, K. M. Krishnan, *J. Magn. Magn. Mater.* **2019**, *471*, 450–456.
- [44] F. A. Tourinho, R. Franck, R. Massart, *J. Mater. Sci.* **1990**, *25*, 3249–3254.
- [45] A. M. Rad, B. Janic, A. Iskander, H. Soltanian-Zadeh, A. S. Arbab, *BioTechniques* **2007**, *43*, 627–636.
- [46] C. S. Johnson, D. A. Gabriel, in *Spectrosc. Biochem.*, CRC Press, Boca-Raton, FL, **2018**, pp. 177–248.
- [47] I. de la Calle, M. Menta, M. Klein, B. Maxit, F. Séby, *Spectrochim. Acta Part B At. Spectrosc.* **2018**, *147*, 28–42.
- [48] J. Wells, O. Kosch, F. Wiekhorst, *J. Magn. Magn. Mater.* **2022**, *563*, 169992.
- [49] E. Bertuit, N. Menguy, C. Wilhelm, A.-L. Rollet, A. Abou-Hassan, *Commun. Chem.* **2022**, *5*, 1–10.
- [50] Á. Gallo-Cordova, A. Espinosa, A. Serrano, L. Gutiérrez, N. Menéndez, M. del Puerto Morales, E. Mazarío, *Mater. Chem. Front.* **2020**, *4*, 3063–3073.
- [51] N. T. K. Thanh, N. Maclean, S. Mahiddine, *Chem. Rev.* **2014**, *114*, 7610–7630.
- [52] L. Lartigue, P. Hugounenq, D. Alloyeau, S. P. Clarke, M. Lévy, J.-C. Bacri, R. Bazzi, D. F. Brougham, C. Wilhelm, F. Gazeau, *ACS Nano* **2012**, *6*, 10935–10949.
- [53] O. Gerber, B. P. Pichon, D. Ihiawakrim, I. Florea, S. Moldovan, O. Ersen, D. Begin, J.-M. Grenèche, S. Lemonnier, E. Barraud, S. Begin-Colin, *Nanoscale* **2016**, *9*, 305–313.
- [54] A. Demortière, P. Panissod, B. P. Pichon, G. Pourroy, D. Guillon, B. Donnio, S. Bégin-Colin, *Nanoscale* **2011**, *3*, 225–232.
- [55] J. Park, E. Lee, N.-M. Hwang, M. Kang, S. C. Kim, Y. Hwang, J.-G. Park, H.-J. Noh, J.-Y. Kim, J.-H. Park, T. Hyeon, *Angew. Chem. Int. Ed.* **2005**, *44*, 2872–2877.
- [56] J. Tang, M. Myers, K. A. Bosnick, L. E. Brus, *J. Phys. Chem. B* **2003**, *107*, 7501–7506.
- [57] J. Judith Vijaya, G. Sekaran, M. Bououdina, *Ceram. Int.* **2015**, *41*, 15–26.
- [58] B. Maibam, S. Baruah, S. Kumar, *SN Appl. Sci.* **2020**, *2*, 1712.

- [59] S. K. Shaw, J. Kailashiya, A. Gangwar, S. K. Alla, S. K. Gupta, C. L. Prajapat, S. S. Meena, D. Dash, P. Maiti, N. K. Prasad, *Appl. Surf. Sci.* **2021**, *560*, 150025.
- [60] S. M. A. Sadat, S. T. Jahan, A. Haddadi, *J. Biomater. Nanobiotechnology* **2016**, *07*, 91–108.
- [61] M. Levy, A. Quarta, A. Espinosa, A. Figuerola, C. Wilhelm, M. García-Hernández, A. Genovese, A. Falqui, D. Alloyeau, R. Buonsanti, P. D. Cozzoli, M. A. García, F. Gazeau, T. Pellegrino, *Chem. Mater.* **2011**, *23*, 4170–4180.
- [62] S. D. Shingte, A. H. Phakatkar, E. McKiernan, K. Nigoghossian, S. Ferguson, R. Shahbazian-Yassar, D. F. Brougham, *Chem. Mater.* **2022**, *34*, 10801–10810.
- [63] E. Garaio, O. Sandre, J.-M. Collantes, J. A. Garcia, S. Mornet, F. Plazaola, *Nanotechnology* **2015**, *26*, 015704.
- [64] A. Lak, S. Disch, P. Bender, *Adv. Sci.* **2021**, *8*, 2002682.
- [65] U. M. Engelmann, *Assessing Magnetic Fluid Hyperthermia : Magnetic Relaxation Simulation, Modeling of Nanoparticle Uptake inside Pancreatic Tumor Cells and in Vitro Efficacy*, Infinite Science Publishing, **2019**.
- [66] J. S. Micha, B. Dieny, J. R. Régnard, J. F. Jacquot, J. Sort, *J. Magn. Magn. Mater.* **2004**, *272–276*, E967–E968.
- [67] I. J. Bruvera, P. Mendoza Zélis, M. Pilar Calatayud, G. F. Goya, F. H. Sánchez, *J. Appl. Phys.* **2015**, *118*, 184304.
- [68] G. Cotin, C. Blanco-Andujar, F. Pertion, L. Asín, J. M. de la Fuente, W. Reichardt, D. Schaffner, D.-V. Ngyen, D. Mertz, C. Kiefer, F. Meyer, S. Spassov, O. Ersen, M. Chatzidakis, G. A. Botton, C. Hénoumont, S. Laurent, J.-M. Greneche, F. J. Teran, D. Ortega, D. Felder-Flesch, S. Begin-Colin, *Nanoscale* **2021**, *13*, 14552–14571.
- [69] K. Wu, D. Su, R. Saha, J. Liu, J.-P. Wang, *J. Phys. Appl. Phys.* **2019**, *52*, 335002.
- [70] S. Mørup, M. Bo Madsen, J. Franck, J. Villadsen, C. J. W. Koch, *J. Magn. Magn. Mater.* **1983**, *40*, 163–174.
- [71] S. Bedanta, W. Kleemann, *J. Phys. Appl. Phys.* **2009**, *42*, 013001.
- [72] P. Bender, J. Fock, C. Frandsen, M. F. Hansen, C. Balceris, F. Ludwig, O. Posth, E. Wetterskog, L. K. Bogart, P. Southern, W. Szczerba, L. Zeng, K. Witte, C. Grüttner, F. Westphal, D. Honecker, D. González-Alonso, L. Fernández Barquín, C. Johansson, *J. Phys. Chem. C* **2018**, *122*, 3068–3077.
- [73] K. Pisane, Effects of Size and Size Distribution on the Magnetic Properties of Maghemite Nanoparticles and Iron-Platinum Core-Shell Nanoparticles, PhD, West Virginia University Libraries, **2015**.
- [74] Y. Komorida, M. Mito, H. Deguchi, S. Takagi, A. Millán, N. J. O. Silva, F. Palacio, *Appl. Phys. Lett.* **2009**, *94*, 202503.
- [75] J. L. Dormann, F. D’Orazio, F. Lucari, E. Tronc, P. Prene, J. P. Jolivet, D. Fiorani, R. Cherkaoui, M. Nogues, *Phys. Rev. B* **1996**, *53*, 14291–14297.
- [76] R. Hergt, S. Dutz, M. Röder, *J. Phys. Condens. Matter* **2008**, *20*, 385214.
- [77] J.-H. Lee, J. Jang, J. Choi, S. H. Moon, S. Noh, J. Kim, J.-G. Kim, I.-S. Kim, K. I. Park, J. Cheon, *Nat. Nanotechnol.* **2011**, *6*, 418–422.
- [78] R. E. Rosensweig, *J. Magn. Magn. Mater.* **2002**, *252*, 370–374.
- [79] J. Carrey, B. Mehdaoui, M. Respaud, *J. Appl. Phys.* **2011**, *109*, 083921.
- [80] J.-P. Fortin, C. Wilhelm, J. Servais, C. Ménager, J.-C. Bacri, F. Gazeau, *J. Am. Chem. Soc.* **2007**, *129*, 2628–2635.
- [81] M. Lévy, C. Wilhelm, J.-M. Siaugue, O. Horner, J.-C. Bacri, F. Gazeau, *J. Phys. Condens. Matter Inst. Phys. J.* **2008**, *20*, 204133.
- [82] C. Martinez-Boubeta, K. Simeonidis, A. Makridis, M. Angelakeris, O. Iglesias, P. Guardia, A. Cabot, L. Yedra, S. Estradé, F. Peiró, Z. Saggi, P. A. Midgley, I. Conde-Leborán, D. Serantes, D. Baldomir, *Sci. Rep.* **2013**, *3*, 1652.
- [83] P. Guardia, R. D. Corato, L. Lartigue, C. Wilhelm, A. Espinosa, M. Garcia-Hernandez, F. Gazeau, L. Manna, T. Pellegrino, **2012**, *6*, 12.
- [84] C. Blanco-Andujar, D. Ortega, P. Southern, Q. A. Pankhurst, N. T. K. Thanh, *Nanoscale* **2015**, *7*, 1768–1775.
- [85] L. Storozhuk, M. O. Besenhard, S. Mourdikoudis, A. P. LaGrow, M. R. Lees, L. D. Tung, A. Gavriilidis, N. T. K. Thanh, *ACS Appl. Mater. Interfaces* **2021**, *13*, 45870–45880.
- [86] N. A. Usov, *J. Appl. Phys.* **2010**, *107*, 123909.

- [87] M. Marciello, V. Connord, S. Veintemillas-Verdaguer, M. A. Vergés, J. Carrey, M. Respaud, C. J. Serna, M. P. Morales, *J. Mater. Chem. B* **2013**, *1*, 5995.
- [88] J. de A. Gomes, M. H. Sousa, F. A. Tourinho, R. Aquino, G. J. da Silva, J. Depeyrot, E. Dubois, R. Perzynski, *J. Phys. Chem. C* **2008**, *112*, 6220–6227.
- [89] E. Bertuit, S. Neveu, A. Abou-Hassan, *Nanomaterials* **2021**, *12*, 119.
- [90] S. Ruta, R. Chantrell, O. Hovorka, *Sci. Rep.* **2015**, *5*, 9090.
- [91] W. J. Atkinson, I. A. Brezovich, D. P. Chakraborty, *IEEE Trans. Biomed. Eng.* **1984**, *BME-31*, 70–75.
- [92] T. Yoshida, K. Enpuku, *AIP Adv.* **2024**, *14*, 075105.

TOC Graphic



A comprehensive study of the multiscale structure-function relationships on a library of iron oxide nanoflowers obtained by the polyol route, relating their nanostructure (number of cores constituting the flower morphology, crystalline defects...) to their magnetic properties: static and dynamic hysteresis loops, magneto-crystalline anisotropy, specific absorption rate: not only particle size but also magnetic field amplitude and frequency matter!